EFFECT OF PHASE NOISE ON THE PERFORMANCE OF COHERENT VISIBLE LIGHT COMMUNICATION SYSTEMS

A Thesis

by

Zeynep Özbilgin

Submitted to the
Graduate School of Sciences and Engineering
In Partial Fulfillment of the Requirements for
the Degree of

Master of Science

in the
Department of Electrical and Electronics Engineering

Özyeğin University
May 2024

EFFECT OF PHASE NOISE ON THE PERFORMANCE OF COHERENT VISIBLE LIGHT COMMUNICATION SYSTEMS

Approved by:

Prof. Murat Uysal, Advisor
Dept. of Electrical & Electronics Eng.
Özyeğin University

Asst. Prof. Çağatay Edemen
Dept. of Electrical & Electronics Eng.
Özyeğin University

Assoc. Prof. Eylem Erdoğan
Dept. of Electrical & Electronics Eng.
Izmir Institute of Technology

Date Approved: May 21, 2024

To my dear family

ABSTRACT

Leveraging the inherent data carrying capability of light-emitting diode (LED) based illumination infrastructure, visible light communication (VLC) offers a promising approach for wireless data transmission. The recent advent of commercially available white-light luminaires equipped with laser diodes (LDs) presents a unique opportunity to realize high-performance coherent VLC systems. In contrast to conventional VLC employing intensity modulation, coherent VLC harnesses the superior bandwidth characteristics of lasers and advanced digital signal processing (DSP) techniques to achieve significantly enhanced data rates. Coherent detection schemes rely on a highly stable, monochromatic laser as a local oscillator (LO). However, practical laser implementations exhibit inherent phase noise stemming from spontaneous emission and carrier density fluctuations. This work presents a comprehensive analysis of the detrimental effects of phase noise on the performance of a coherent VLC system. To counteract the detrimental effects of phase noise, we propose the utilization of a phase-locked loop (PLL). By characterizing the statistical distribution of the residual phase error after PLL operation, we derive an approximate closed-form expression for the pairwise error probability (PEP). Subsequently, a union bound is established to quantify the overall bit error rate (BER). The derived analytical framework is validated through extensive simulations, confirming its accuracy and enabling the quantification of phase noise's effect on the system's error rate performance.

ÖZETÇE

Görünür ışık iletişimi (VLC), LED tabanlı aydınlatma altyapısının veri taşıma yeteneğinden faydalanaran, kablosuz iletişim için gelecek vadeden bir yaklaşımdır. Lazer diyot (LD) ile donatılmış beyaz ışık aydınlatmalarının ticari olarak piyasaya sürülmesi, yüksek performanslı eş evreli VLC sistemlerinin geliştirilmesi için eşsiz bir fırsat sunmaktadır. Geleneksel yoğunluk modülasyonu kullanan VLC'den farklı olarak, eş evreli VLC, lazerlerin üstün bant genişliği özelliklerini ve gelişmiş dijital sinyal işleme (DSP) tekniklerini kullanarak veri hızlarını önemli ölçüde artırır. Eş evreli alıcı şemaları oldukça stabil davranan tek renkli bir lazere lokal osilatör (LO) olarak ihtiyaç duyar. Ancak, lazerlerin gerçek uygulamalarında kendiliğinden emisyon ve taşıyıcı yoğunluğu dalgalanmaları nedeniyle faz gürültüsü oluşur. Bu çalışma, faz gürültüsünün tutarlı bir VLC sisteminin performansı üzerindeki olumsuz etkilerini kapsamlı bir şekilde analiz eder. Faz gürültüsünün olumsuz etkilerini azaltmak için bir faz kilitlemeli döngü (PLL) kullanılmasını öneriyoruz. PLL işleminden sonra kalan faz hatasının istatistiksel dağılımını karakterize ederek, çiftsel hata olasılığı (PEP) için yaklaşık bir kapalı form ifade türetiyoruz. Daha sonra, toplam bit hata oranını (BER) hesaplamak için bir birleşim sınırı oluşturulur. Elde edilen analitik ifadeler, kapsamlı simülasyonlarla onaylanarak doğruluk oranı teyit edilir ve faz gürültüsünün sistemin hata oranı performansı üzerindeki etkisi incelenir.

# ACKNOWLEDGEMENTS

First and foremost, I would like to express my deepest appreciation to my supervisor, Prof. Murat Uysal, for his invaluable guidance, patience, and encouragement throughout the entire research process. His expertise, constructive feedback, and unwavering support have been instrumental in shaping this thesis.

I extend my sincerest gratitude to the esteemed members of my dissertation committee, Asst. Prof. Çağatay Edemen and Assoc. Prof. Eylem Erdoğan, for their invaluable insights and unwavering commitment in reviewing my thesis.

My heartfelt thanks go to my parents, İsmail and Tuba, for their unwavering support, love, and encouragement throughout my academic pursuits. Special thanks to my siblings, Kübra and Furkan, their understanding, patience, and belief in my abilities have been my source of strength and motivation.

Last but not least, I am deeply thankful to my friends and colleagues for their encouragement, understanding, and moral support during this challenging yet rewarding journey.

TABLE OF CONTENTS

LIST OF TABLES

LIST OF FIGURES

CHAPTER I

INTRODUCTION

1.1 Motivation

The advancements in digital technologies gave rise to higher data transmission rates and wider bandwidths in order to compensate for higher number of users and data intensive applications. Therefore, in the last few decades, there is an increasing demand in radio frequency (RF) spectrum. According to [1], the spectrum is expected to be fully congested around 2035. Several studies, investigating the limits of spectrum allocation, point out an emergent need for alternative technologies in realm of 5G and beyond systems. Considering this, Visible Light Communication (VLC) has been found to be a promising technology for next generation wireless communication systems [1, 2, 3]. In comparison to existing RF technologies, VLC is more advantageous in terms of several aspects: (i) bandwidth, (ii) safety, (iii) privacy, (iv) efficiency [4]. While RF spectrum ranges from 3 kHz to 300 GHz, visible light spectrum ranges between 400-800 THz yielding 1,000 times wider bandwidth free of reservation charge [5]. Since VLC does not suffer from interference and emits harmful radiations unlike radio waves, it provides more secure and safer transmission [6]. Moreover, the existing lighting infrastructure allows for efficient implementation by combining low energy and cheap illumination modules with communication [7]. In consequence of these benefits, the need for high data rate communication, and dwindling RF spectrum makes VLC more favorable for many applications as a complementary technology.

Visible Light Communication represents a cutting-edge technology that harnesses the modulation of visible light wavelengths to enable high-speed wireless communication. This innovative approach capitalizes on existing illumination infrastructures, effectively transforming each light source into a potential transmitter. VLC's promise lies in its ability to offer rapid and widespread indoor wireless access, particularly in densely populated environments, thereby positioning itself as a complementary solution alongside traditional radio frequency (RF) systems. Over the past decade, VLC has garnered significant attention, fueling a surge in research endeavors aimed at unlocking its vast potential. Comprehensive surveys [8] attest to the growing interest and exploration within the field. While the predominant assumption in current literature is that VLC systems rely on light emitting diodes (LEDs) as transmitters due to their ubiquitous deployment, LEDs do pose inherent limitations. Notably, their low-pass frequency response restricts available electrical bandwidth to a few megahertz, albeit this can be expanded to tens of megahertz through pre-equalization schemes [9, 10]. However, the demands of emerging applications, such as extended reality, mobile holography, and digital twins, necessitate data rates surpassing the capabilities of conventional LED-based VLC systems. Requirements reaching up to 1 terabit per second (Tbps) mandate bandwidths ranging from hundreds of megahertz to tens of gigahertz, aligning with the performance benchmarks envisioned for 6G and beyond networks [11]. To bridge this gap, VLC must evolve, addressing the bandwidth limitations imposed by traditional light sources. With the invention of laser-based white lighting, a promising alternative poised to unlock VLC's full potential. Early examples of laser diode (LD)-powered white luminaires are already making strides in automotive applications [12] and are anticipated to supplant LEDs in residential and commercial settings [13]. LD-based white light sources boast significantly higher electrical bandwidths, scaling up to several gigahertz, compared to their LED counterparts. Initial experimental endeavors [14, 15, 16, 17, 18, 19, 20] have showcased the feasibility of achieving data rates in the tens of gigabits per second (Gbps) range with LD-based white light sources.

In this study, we consider a coherent VLC system with an LD-based white light luminary and analyze its performance in the presence of phase noise. The laser phase noise is characterized by Wiener process whereas the phase estimate error is modeled with Gaussian process. We consider M-ary phase shift keying (M-PSK) and derive a closed-form expression for the pairwise error probability (PEP). Building on the PEP, we provide a union bound on the error probability. We further confirm the accuracy of our derivations through extensive Monte Carlo simulations.

1.2 Thesis Outline

The rest of the thesis report is organized as follows: In Chapter 2, we present a comprehensive literature review on the topic and the novelty of this study. In Chapter 3, we present our system model under consideration. In Subchapter 3.1, transceiver architecture is mentioned. In Subchapter 3.2, we discuss the models of laser phase noise and residual phase error after the phase recovery process. The details of phase recovery process is explained in Subchapter 3.2.1. Next, the simulation parameters are given with proper explanations in Subchapter 3.3. In Subchapter 3.4, we provide the details of PEP derivation and present the union bound which is laying the groundwork for this study. In Chapter 4, we present the numerical results and verify our analytical findings with the simulation results. Finally, we conclude our work by summarizing key insights in Chapter 5.

1.3 Notation

$\mathrm{Re}\{\cdot\}$ and $\mathrm{E}\{\cdot\}$ denote real part and expectation operations. j denotes $\sqrt{-1}$. $N(\cdot)$ and $CN(\cdot)$ respectively stand for Gaussian distribution and complex Gaussian distribution. $LN(\cdot)$ denotes lognormal distribution. $\|\cdot\|$, $(\cdot)^*$, $(\cdot)^{\mathrm{T}}$ and $(\cdot)^{\mathrm{H}}$ respectively stand for the norm, conjugate, transpose and Hermitian transpose operations, respectively. Bold letters are used for vector notation.

CHAPTER II

LITERATURE REVIEW

2.1 Intensity Modulation and Direct Detection

In the current literature, VLC systems typically build upon intensity modulation and direct detection (IM/DD), where the information is encoded in the intensity of light source and then retrieved by a photodetector via envelope detection. This modulation technique simplifies the transmitter design and is often implemented using straightforward modulation formats like On-Off Keying (OOK) or Pulse Position Modulation (PPM) [21]. At the receiver, only the intensity of the received optical signal is detected, without extracting phase information. This approach simplifies receiver design and reduces costs. IM/DD schemes are commonly used in optical communication systems where simplicity, cost-effectiveness, and moderate to high data rates over relatively short distances are priorities. However, they may be susceptible to impairments such as dispersion, ambient light interference, and noise, which can limit their performance, especially in long-haul or high-speed communication scenarios [22]. Despite these limitations, IM/DD schemes remain popular for applications such as short-range optical wireless communication, access networks, and point-to-point links [23]. Such a choice is dictated by the non-coherent nature of LED sources. LED-VLC concept is studied comprehensively and utilized in diverse fields such as health monitoring, indoor navigation, home automation, intelligent transportation [24, 25, 26, 27, 28]. In general, the utilization of IM/DD helps mitigating the occurrence of multipath fading, primarily due to the transmission wavelength and detector area. Nevertheless, it inherently comes with limitations on maximum achievable data rate and inadequate modulation schemes. These drawbacks preclude the LEDs from

Table 1: Comparison of IM/DD and coherent schemes

	IM/DD	**Coherent**
Modulation Types	Intensity	Amplitude and phase
Detection Method	Direct	Homodyne or heterodyne
Sensitivity to Carrier Phase	No	Yes
Sensitivity to Polarization	No	Yes

becoming an optimal implementation of VLC and promote the search of improved light sources.

2.2 Coherent Detection

In coherent optical communication schemes, data is transmitted and received using both the amplitude and phase of the optical carrier signal. This allows for more complex modulation formats such as Quadrature Amplitude Modulation (QAM) or Differential Phase Shift Keying (DPSK) to be employed, which can achieve higher spectral efficiency and better tolerance to impairments. At the receiver, coherent detection is used to recover both the amplitude and phase information of the received optical signal, enabling advanced digital signal processing (DSP) techniques to enhance performance. Coherent schemes are commonly used in long-haul optical communication networks where high data rates and transmission distances are required. However, they are more complex and expensive compared to IM/DD schemes, making them less suitable for applications where simplicity and cost-effectiveness are prioritized. Coherent optical communication systems find applications in submarine communication cables, data center interconnects, and high-speed telecommunications networks. A general comparison of IM/DD vs coherent schemes are given in Table 1. The transceiver block diagrams of non-coherent and coherent schemes are given in Fig. 1 and Fig. 2, respectively.

On the other hand, LDs are coherent light sources and allow the implementation of coherent VLC systems. Coherent VLC systems can leverage the high bandwidth

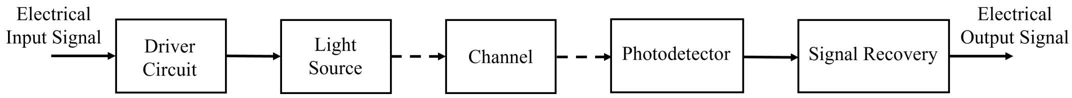

Figure 1: A general transceiver architecture for a non-coherent scheme

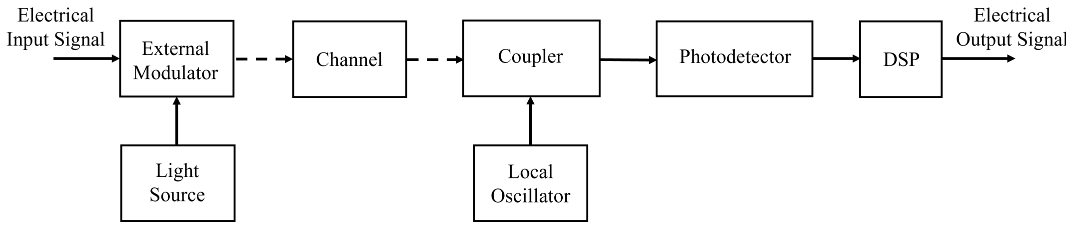

Figure 2: A general transceiver architecture for a coherent scheme

of lasers and advanced DSP to push the data rates in the order of Tbps. Coherent techniques have already become the de-facto standard for 100G and beyond fiber optic links [29] and also explored for free space optical links at infrared wavelengths [30]. There are many experimental studies which demonstrate high speed transmission utilizing different modulation schemes at different distances using LDs in the scale of gigabits [16, 17, 18, 19, 20, 31, 32, 33, 34, 35]. Most of them propose to use single wavelength LDs enabling point-to-point communication [31, 33, 34, 35] for application scenarios including free-space and underwater [34, 35]. However, despite the exceptional luminance of high-power LDs, they pose significant risk for eye safety restricting its real-life daily usage. On the other hand, the invention of white light emission utilizing the combination of blue LD with yellow phosphor provides significant advantages [36]. The diffusing effect of the phosphor material generates an eye safe white light emission which provides flexibility for the applications of communication.

[16, 17, 18, 19, 20] utilizes this technology and demonstrates remarkable results. [16] and [17], achieving 2 Gbit/s and 5.2 Gbit/s respectively, showed the potential of laser-based phosphor-converted white lighting systems for high data rate VLC without the need for RGB lasers or an additional optical filter. [18] showed that 10 Gbit/s is achievable by employing a two-channel imaging system and gave a considerable promise that LD based white lighting system contributes to VLC. Next, [19] showed that using an LD based white light SMD source offers high design flexibility and achieve extremely high data rates of over 20 Gbit/s by utilizing both OFDM and WDM. In the most recent study [20], a novel configuration of LD based Li-Fi system achieving a maximum of 26 Gbit/s over a free space distance of 3 m by a single SMD is proposed. They showed the viability of scaling the data rate by integrating multiple LDs at the transmitter without adding substantial complexity to the system.

However, comprehensive investigation of coherent VLC architectures particularly in the presence of practical hardware imperfections has not been reported in the literature. A typical digital coherent optical receiver is composed of an optical front-end followed by baseband processing. The optical front-end (also referred to as IQ coherent receiver in the fiber optic literature) can be implemented either as a single-branch or dual-branch (i.e., balanced) the latter of which provides superior suppression of the DC component and a higher power efficiency. At the receiver front-end, a local oscillator in the form of a monochromatic laser is used. In practice, lasers suffer from random fluctuations in phase due to spontaneous emission and carrier density fluctuations [37]. While the effect of phase noise was explored in coherent fiber optic systems [38, 39, 40] and free space optical systems [41, 42], this was not yet investigated in the context of VLC which provides the motivation of our study.

CHAPTER III

SYSTEM MODEL

In this chapter, the overall system model will be introduced. First of all, transceiver architecture is explained. The designed system will be analyzed further including the phase noise factor. We also mention and discuss about how to compensate such phase noise. Then, we model the phase recovery error. Furthermore, we give the simulation parameters. Based on the derived system model, a closed form solution for error probability will be investigated and a novel approximation method is proposed.

3.1 Transceiver Architecture

The block diagrams of transmitter and receiver architectures are respectively presented in Fig. 3 and Fig. 4. At the transmitter side (Fig. 3), the optical field generated by the laser source can be expressed as $\sqrt{2}A_c \cos\left(2\pi f_c t + \theta_c(t)\right)$ where f_c is the operation frequency, A_c is the amplitude, $\theta_c(t)$ is the phase noise and $\sqrt{2}$ is used to normalize the energy of the carrier signal. After the beam splitter which introduces a 3 dB loss, the resulting signals are fed into an optical IQ modulator with one Mach-Zender Modulator (MZM) in each branch. Let $v_I(t)$ and $v_Q(t)$ denote the

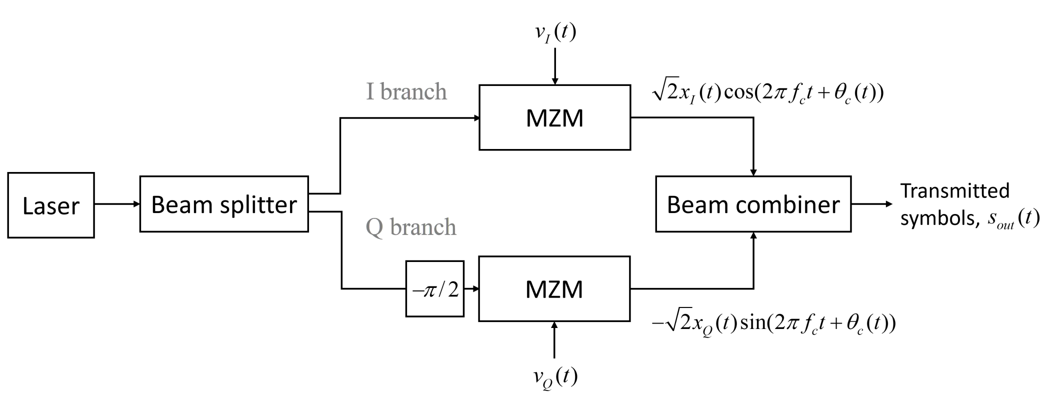

Figure 3: Block diagram of coherent VLC transmitter for M-PSK signal generation

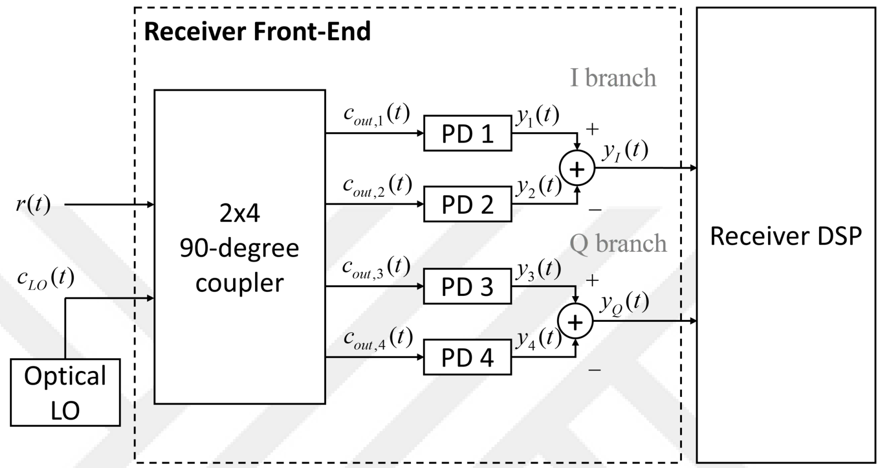

(a)

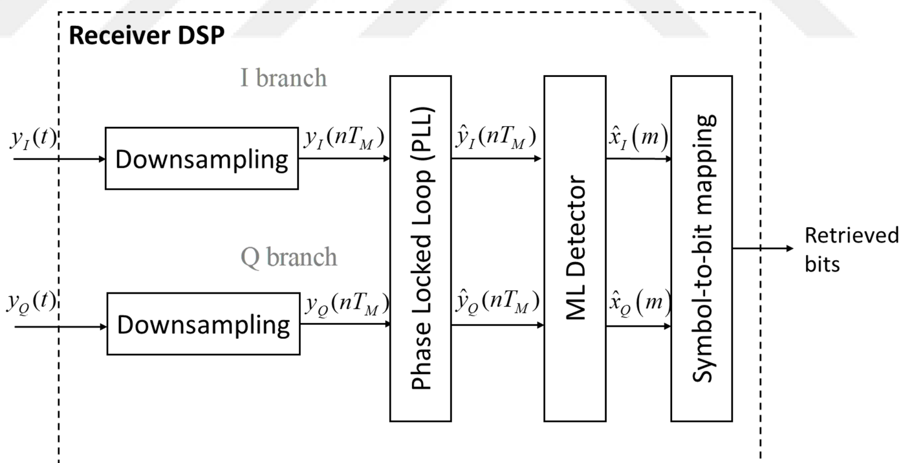

(b)

Figure 4: a) Overall block diagram of coherent VLC receiver b) Sub-blocks of receiver DSP block

modulating voltage signals applied to the in-phase and quadrature MZMs to generate the desired M-PSK symbol $x(t)$. In the following, we assume $A_c = \sqrt{2}$ to have unit power M-PSK symbols. The baseband signal representations of the symbol on I and Q branches can be written as

$$x_I(t) = \cos\left[\frac{\pi}{V_\pi}\left(v_I(t) - \frac{V_{bias}}{2}\right)\right] \tag{1}$$

$$x_Q(t) = \cos\left[\frac{\pi}{V_\pi}\left(v_Q(t) - \frac{V_{bias}}{2}\right)\right] \tag{2}$$

where V_{bias} is the bias voltage and V_π is the reference voltage that generates a π radian displacement in the phase. Hereby, we can set $V_{bias} = V_\pi$ in (1) and (2) to ensure that the amplitude of $x_I(t)$ and $x_Q(t)$ varies between $[-1, 1]$. Any M-PSK signal can be formed by adjusting the levels of $v_I(t)$ and $v_Q(t)$ with a $2\pi/M$ phase shift, where M is the modulation order. Mathematically speaking, they are selected as

$$v_I(t) = p(t)V_\pi\left(\frac{\cos^{-1}(\cos(\theta_m))}{\pi} + \frac{1}{2}\right) \tag{3}$$

$$v_Q(t) = p(t)V_\pi\left(\frac{\cos^{-1}(\sin(\theta_m))}{\pi} + \frac{1}{2}\right) \tag{4}$$

where $\theta_m \in \{2\pi m/M, m = 1, 2..M\}$ and $v_{I,Q}(t) \in [-V_\pi/2, V_\pi/2]$. $p(t)$ is non-return-to-zero rectangular pulse shape. The outputs of MZM branches are then combined together to produce the output of the transmitter as

$$s_{out}(t) = \sqrt{2}x_I(t)\cos(2\pi f_c t + \theta_c(t)) - \sqrt{2}x_Q(t)\sin(2\pi f_c t + \theta_c(t)) \tag{5}$$

This can be rewritten as

$$s_{out}(t) = \sqrt{2}\mathrm{Re}\{\tilde{s}_{out}(t)\} \tag{6}$$

where $\tilde{s}_{out} = x(t)e^{-j(2\pi f_c t + \theta_c(t))}$ is the complex envelope of the transmitted signal and $x(t) = x_I(t) - jx_Q(t) = e^{-j\theta_m(t)}$ is the baseband M-PSK signal. Even tough complex exponentials are not realistic to represent signals, we can utilize them for mathematical tractability. The real-valued implementation of the signal modeling is explained in Appendix A.

The transmitted signal goes through the propagation channel. In a typical indoor environment, the VLC channel is deterministic in nature and basically provides an attenuation factor which will be ignored in this study for the simplicity of presentation. The received signal takes the form of

$$\tilde{r}(t) = \tilde{s}_{out}(t) + z(t) \tag{7}$$

where $z(t)$ is the additive thermal noise. It is modeled by Gaussian distribution where real and imaginary parts are independently modeled as a zero mean normal distribution. The variance of each quadrature part equals to the half of the complex noise power, i.e., $z_{\mathrm{Re}}, z_{\mathrm{Im}} \sim N(0, N_0/2)$.

At the receiver side (Fig. 2), the optical front-end architecture mixes the received signal $r(t) = \mathrm{Re}\{\tilde{r}(t)\}$ with the optical local oscillator (LO) signal given in the real form by $c_{LO}(t) = \sqrt{2}\mathrm{Re}\left\{A_{LO}e^{-j(2\pi f_{LO}t+\theta_{LO}(t))}\right\}$ where A_{LO} is the amplitude, f_{LO} is the frequency, and $\theta_{LO}(t)$ is the phase noise of the laser. For the mixing process, we use a 2x4 90-degree coupler which takes the form

$$\mathbf{T} = \frac{1}{2}\begin{bmatrix} 1 & 1 \\ 1 & e^{j\pi} \\ 1 & e^{j\pi/2} \\ 1 & e^{j3\pi/2} \end{bmatrix} \tag{8}$$

The output of the coupler is given by

$$\begin{bmatrix} c_{out,1}(t) \\ c_{out,2}(t) \\ c_{out,3}(t) \\ c_{out,4}(t) \end{bmatrix} = \mathbf{T}\begin{bmatrix} \tilde{r}(t) \\ \tilde{c}_{LO}(t) \end{bmatrix} = \begin{bmatrix} \left(\tilde{r}(t) + \tilde{c}_{LO}(t)\right)/2 \\ \left(\tilde{r}(t) + e^{j\pi}\tilde{c}_{LO}(t)\right)/2 \\ \left(\tilde{r}(t) + e^{j\pi/2}\tilde{c}_{LO}(t)\right)/2 \\ \left(\tilde{r}(t) + e^{j3\pi/2}\tilde{c}_{LO}(t)\right)/2 \end{bmatrix} \tag{9}$$

Each of the four coupler outputs is applied to a separate photodetector. The resulting photocurrents are given by

$$y_i(t) = R|c_{out,i}(t)|^2, \quad i = 1, 2, 3, 4 \tag{10}$$

where R is photodetector responsivity. The output current on I branch is obtained as

$$\begin{aligned} y_I(t) =& y_1(t) - y_2(t) \\ =& R|0.5\tilde{r}(t) + 0.5\tilde{c}_{LO}(t)|^2 - R\left|0.5\tilde{r}(t) + 0.5e^{j\pi}\tilde{c}_{LO}(t)\right|^2 \\ =& \mathrm{Re}\left\{R\tilde{r}(t)\tilde{c}^*_{LO}(t)\right\} \end{aligned} \tag{11}$$

where we have used $|a+b|^2 = |a|^2 + |b|^2 + 2\mathrm{Re}\{ab^*\}$. Similarly, the output current on Q branch is obtained as

$$\begin{aligned} y_Q(t) =& y_3(t) - y_4(t) \\ =& R\left|0.5\tilde{r}(t) + 0.5e^{j\pi/2}\tilde{c}_{LO}(t)\right|^2 - R\left|0.5\tilde{r}(t) + 0.5e^{j3\pi/2}\tilde{c}_{LO}(t)\right|^2 \\ =& \mathrm{Re}\left\{R\tilde{r}(t)\tilde{c}^*_{LO}(t)e^{-j\pi/2}\right\} \end{aligned} \tag{12}$$

Replacing $r(t)$ and $c_{LO}(t)$ in (11) and (12), we obtain noisy baseband signal components as in (13) and (14).

$$y_I(t) = \mathrm{Re}\left\{RA_{LO}e^{-j(2\pi(f_c - f_{LO})t + \theta_c(t) + \theta_m(t) - \theta_{LO}(t))} + z(t)RA_{LO}e^{j(2\pi f_{LO}t + \theta_{LO}(t))}\right\} \tag{13}$$

$$y_Q(t) = \mathrm{Re}\left\{RA_{LO}e^{-j(2\pi(f_c - f_{LO})t + \theta_c(t) + \theta_m(t) - \theta_{LO}(t) + \pi/2)} + z(t)RA_{LO}e^{j(2\pi f_{LO}t + \theta_{LO}(t) - \pi/2)}\right\} \tag{14}$$

Note that only the lower frequency (i.e., $f_{LO} - f_c$) component of the downconverted signal is present at the output of the photodetector because the higher frequency component (i.e., $f_{LO} + f_c$) is eliminated by the photodetector's frequency response. Please see Appendix A to refer non-complex representation of downconversion operation. It is proved that complex representation is optimal since it already does the filtering operation.

Combining the resulting signals in two branches and further assuming perfect frequency synchronization, i.e., $f_{LO} = f_c$. Frequency synchronization is performed using timing or non-timing aided methods in practice. The operations can be done in two steps as coarse and fine synchronization to provide a fast convergence and reduced locking time even in the presence of large frequency offset values [43], [44]. Then, we obtain

$$\begin{aligned} y(t) &= y_I(t) + jy_Q(t) \\ &= RA_{LO}e^{-j(\theta_m(t)+\theta_n(t))} + RA_{LO}z'(t) \end{aligned} \tag{15}$$

where $\theta_n(t) = \theta_c(t) - \theta_{LO}(t)$ is the overall phase noise and $z'(t) = z(t)e^{j(2\pi f_{LO}t+\theta_{LO}(t))}$.

Let N and T_s, respectively, denote the number of transmitted symbols and the sample period. For baseband processing, the output electrical signal is downsampled by L to obtain the symbol at the k^{th} index $y(kT_M)$ $k = 1, 2, ..N$ where T_M stands for single symbol period and is equal to LT_s. The downsampled signal is then passed through a phase recovery unit to recover the phase mismatch. Let $\hat{\theta}_n(kT_M)$ denote the estimate of the phase noise. After phase recovery, the signal takes the form of

$$\begin{aligned} \hat{y}(kT_M) &= y(kT_M)e^{j\hat{\theta}_n(kT_M)} \\ &= RA_{LO}e^{-j(\theta_m(kT_M)+\theta_{err}(kT_M))} + RA_{LO}z''(kT_M) \end{aligned} \tag{16}$$

where $\theta_{err}(kT_M) = \theta_n(kT_M) - \hat{\theta}_n(kT_M)$ is the residual phase noise and $z''(kT_M) = z'(kT_M)e^{j\hat{\theta}_n(kT_M)}$ is the effective complex noise term. Due to the symmetry of complex Gaussian distribution, phase rotation does not change the distribution of noise, therefore we have $z, z', z'' \sim CN(0, N_0)$. The received signal vector can be then written as

$$\hat{\mathbf{y}} = RA_{LO}\left(e^{-j(\boldsymbol{\theta}_{\mathbf{m}}+\boldsymbol{\theta}_{\mathbf{err}})} + \mathbf{z}''\right) \tag{17}$$

where $\boldsymbol{\theta}_m = \left[\theta_m(T_M), \theta_m(2T_M) ... \theta_m(NT_M)\right]^{\mathrm{T}}$, $\mathbf{z}'' = \left[z''(T_M), z''(2T_M) ... z''(NT_M)\right]^{\mathrm{T}}$, and $\boldsymbol{\theta}_{err} = \left[\theta_{err}(T_M), \theta_{err}(2T_M) ... \theta_{err}(NT_M)\right]^{\mathrm{T}}$.

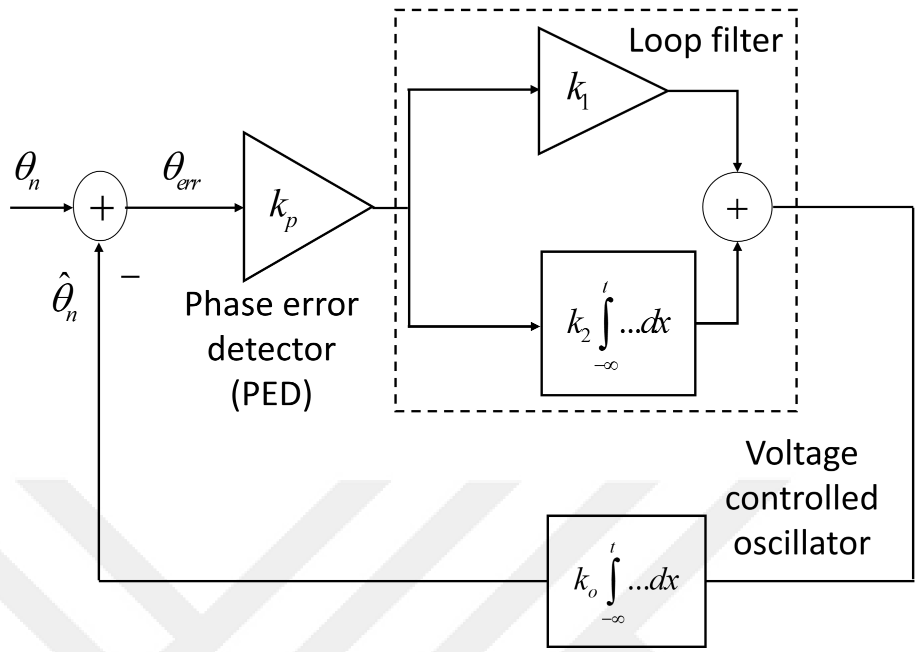

Figure 5: Block diagram of linearized phase equivalent PLL

Let $\mathbf{X} = [x_1, x_2...x_N]^{\mathrm{T}}$ denote the baseband transmitted signal vector where $x_k = e^{-j\theta_m(kT_M)}$, $k = 1, 2, ..N$. The decision is made based on the maximum likelihood (ML) metric that takes the form of

$$\hat{\mathbf{X}} = \underset{x_1, x_2 ... x_M}{\arg\min} \left\| \hat{\mathbf{y}} - \mathbf{X} \right\|^2 = \underset{x_1, x_2 ... x_M}{\arg\max} \left(\mathrm{Re} \left\{ \hat{\mathbf{y}}^{\mathrm{H}} \mathbf{X} \right\} \right) \tag{18}$$

where $\hat{\mathbf{X}} = [\hat{x}_1, \hat{x}_2 ... \hat{x}_N]^{\mathrm{T}}$ is the retrieved signal vector.

3.2 Modeling of Phase Noise

The phases of transmitter and receiver oscillators manifest independent random rotations and distort the constellation inevitably. Laser phase noise is typically modeled as continuous Wiener random process [45] such that phase difference between two samples collected τ seconds apart is described by Gaussian distribution with zero mean and variance $\sigma^2 = 2\pi\Delta v \left|\tau\right|$ where Δv denotes the laser linewidth. In our case, the received signal has an overall phase noise of $\theta_n(t) = \theta_c(t) - \theta_{LO}(t)$ manifesting a combined Wiener process. The variance of the resulting phase is therefore found by ${\sigma_n}^2 = 2\pi \left(\Delta v_c + \Delta v_{LO}\right) \left|\tau\right|$ where Δv_c and $\Delta v_{_{LO}}$ are linewidths of transmitter and

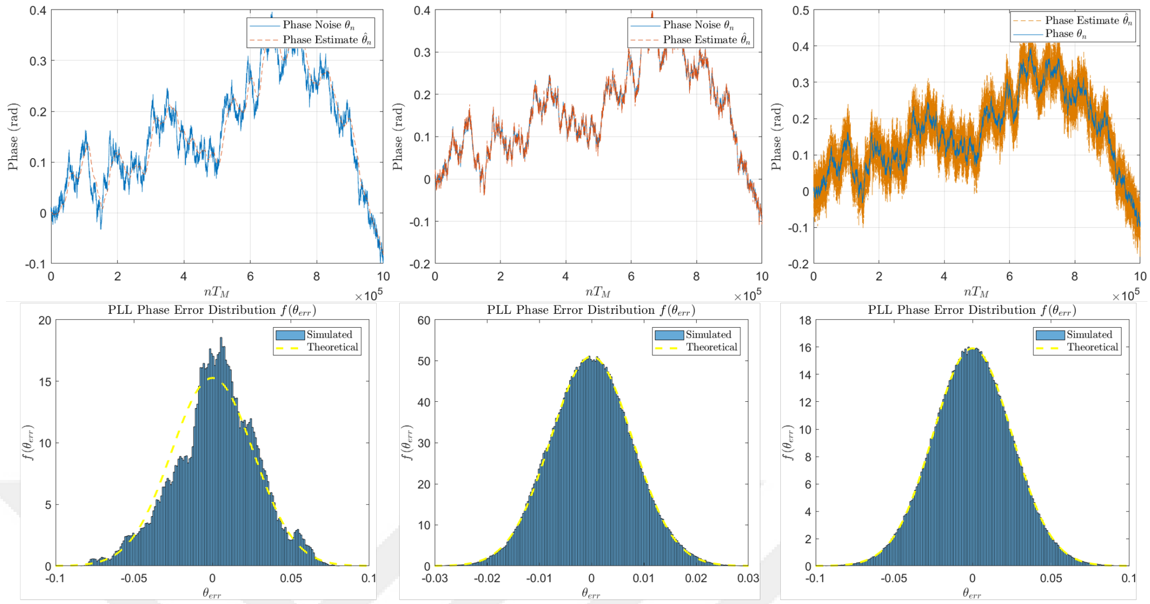

(a) $B_n = 0.00001,\ \sigma_{err}^2 = 6.82\times10^{-4}$ **(b)** $B_n = 0.0006,\ \sigma_{err}^2 = 6.10\times10^{-5}$ **(c)** $B_n = 0.005,\ \sigma_{err}^2 = 6.28\times10^{-4}$

Figure 6: Phase noise for different values: The figures in the first row present input and output phase of the PLL with respect to symbol timing. The figures in the second row present the histograms of residual phase error.

receiver carriers, respectively [45]. In practical implementation, these phase rotations are compensated by utilizing phase recovery algorithms in receiver DSP chain. The statistical distribution of the residual phase depends on the phase recovery method. In the following, we assume the use of a data-aided phase locked loop (PLL) for phase recovery purposes.

3.2.1 Phase Locked Loop Design

A PLL is used to synchronize a periodic waveform with a reference periodic waveform. It tracks the phase and frequency of an incoming sinusoid. It is composed of 3 main components: Phase error detector (PED), loop filter and voltage controlled oscillator (VCO).

As illustrated in Fig. 5, the PLL receives the downsampled photodetector current signal as input and updates the phase of the current symbol based on the detected phase error in the previous symbol. The phase error is filtered by a loop filter to produce a control voltage that adjusts the phase of the VCO. The input-output relationship of a PED is a nonlinear function that typically follows an S shape. However, for sufficiently small θ_{err}, this can be approximated as a linear function. Accordingly, the PED output is given by $k_p \theta_{err}$ where k_p is the PED gain. To achieve a zero steady-state phase error and fine tracking process, a proportional-plus-integrator loop filter with the parameters of k_1 and k_2 is used. Output phase of the VCO is calculated by integrating the loop filter output with a gain factor of k_o. Overall, the PLL is designed to adjust the control voltage such that it produces a phase estimate that drives the phase error to zero.

$$\theta_{err}(t) > 0 \rightarrow \theta_n(t) > \hat{\theta}_n(t) \tag{19}$$

$$\theta_{err}(t) < 0 \rightarrow \theta_n(t) < \hat{\theta}_n(t) \tag{20}$$

If the condition in (19) is hold, these are the actions carried out by VCO:

- The phase of VCO output lags the PLL input and must be increased.
- The positive phase error produces a positive control voltage.
- The positive control voltage increases the phase of the VCO output.

If the condition in (20) is hold, these are the actions carried out by VCO:

- The phase of VCO output is ahead of the PLL input and must be decreased.
- The negative phase error produces a negative control voltage.
- The negative control voltage decreases the phase of the VCO output.

In the PLL design, normalized loop bandwidth (B_n) and damping factor (ζ) should be chosen considering the trade off between fast lock time and reduced tracking error. The damping factor controls the level of oscillatory behaviour in the phase acquisition process [46]. There are 3 levels classified for ζ:

- Underdamped ($\zeta < 1$): The loop response exhibits damped oscillations in the form of overshoots and undershoots.

- Overdamped ($\zeta > 1$): The loop response is the sum of decaying exponentials and oscillatory behaviour disappears.

- Critically damped ($\zeta = 1$): The loop response is somewhere between damped oscillations and decaying exponentials.

Then, the filter parameters are set as [47]

$$k_1 = \frac{1}{k_o k_p} \frac{4\zeta w_n}{1 + 2\zeta w_n + w_n^2} \tag{21}$$

$$k_2 = \frac{1}{k_o k_p} \frac{4 w_n^2}{1 + 2\zeta w_n + w_n^2} \tag{22}$$

where w_n is the normalized natural frequency and can be calculated by

$$w_n = \frac{B_n}{\zeta + 1/4\zeta} \tag{23}$$

3.3 Simulation Parameters

In the following, we present numerical results to demonstrate the statistical behavior of PLL output. We consider an operation wavelength of 1550 nm which corresponds to $f_c = f_{LO} \approx 1.9 \times 10^{14}$ Hz. We assume the transmission of $N = 10^6$ QPSK symbols (i.e., $M = 4$) with $L = 16$ samples per symbol. Unless mentioned otherwise, we assume combined linewidth of the lasers to be $\Delta v = 1$ MHz. The PLL has PED gain of $k_p = 1/2$, VCO gain of $k_o = 1$, and damping factor of $\zeta = 1$ which corresponds to critically damped behavior. We assume that the received signal-to-noise ratio (SNR) per bit is equal to 10 dB.

In Fig. 6, we present the output phase of PLL along with the input phase and residual phase for different values of normalized loop bandwidth, i.e., $B_n = 10^{-5}$, $B_n = 6 \times 10^{-4}$, and $B_n = 5 \times 10^{-3}$. It is observed that the distribution of residual phase error can be well approximated with a Gaussian distribution when PLL is assumed to be in locked position. Mathematically speaking, it is given by

$$f(\theta_{err}) = \frac{1}{\sigma_{err}\sqrt{2\pi}} e^{\left(-\frac{\theta_{err}{}^2}{2\sigma_{err}{}^2}\right)} \tag{24}$$

It is observed from Fig. 6 that the distribution parameters depend on the value of normalized loop bandwidth. While the mean is approximately zero for all cases, the variance values are found as 6.82×10^{-4}, 6.10×10^{-5}, and 6.28×10^{-4}, respectively for $B_n = 10^{-5}$, $B_n = 6 \times 10^{-4}$, and $B_n = 5 \times 10^{-3}$. Selecting a large B_n results in fastest tracking response but leads to increased noise sensitivity and error margin (Fig. 6.c). For small B_n, on the other hand, phase estimate is robust to noise due to delayed response which also results in more error margin (Fig. 6.a). When B_n is set properly, the random walk of the input phase is tracked perfectly with a negligible time delay (Fig. 6.b).

3.4 Derivation of PEP

Let $P\left(\mathbf{X} \rightarrow \hat{\mathbf{X}}\right)$ denote the PEP when $\hat{\mathbf{X}}$ is erroneously decoded instead of the originally transmitted codeword vector of $\mathbf{X}$. The conditional PEP, i.e., conditioned on the phase estimate error $\boldsymbol{\theta}_{err}$, can be written as

$$P\left(\mathbf{X} \rightarrow \hat{\mathbf{X}} \middle| \boldsymbol{\theta}_{err}\right) = P\left(\mathrm{Re}\left\{\hat{\mathbf{y}}^{\mathrm{H}}\hat{\mathbf{X}}\right\} > \mathrm{Re}\left\{\hat{\mathbf{y}}^{\mathrm{H}}\mathbf{X}\right\} \middle| \boldsymbol{\theta}_{err}\right) \tag{25}$$

By substituting (17) in (25), we have

$$\begin{aligned} &P\left(\mathbf{X} \rightarrow \hat{\mathbf{X}} \middle| \boldsymbol{\theta}_{err}\right) \\ &= P\left(\mathrm{Re}\left\{RA_{LO}e^{j(\theta_m+\theta_{err})^{\mathrm{T}}}\left(\hat{\mathbf{X}}-\mathbf{X}\right) + RA_{LO}(\mathbf{z}'')^{\mathrm{H}}\left(\hat{\mathbf{X}}-\mathbf{X}\right)\right\} > 0 \middle| \boldsymbol{\theta}_{err}\right) \end{aligned} \tag{26}$$

Rearranging the terms, we can rewrite (26) as

$$P\left(\mathbf{X} \rightarrow \hat{\mathbf{X}} \middle| \boldsymbol{\theta}_{err}\right) = P\left(v > \mathrm{Re}\left\{e^{j(\boldsymbol{\theta}_m+\boldsymbol{\theta}_{err})^{\mathrm{T}}}\left(\mathbf{X}-\hat{\mathbf{X}}\right)\right\} \middle| \boldsymbol{\theta}_{err}\right) \tag{27}$$

where $v = \mathrm{Re}\left\{(\mathbf{z}'')^{\mathrm{H}}\left(\hat{\mathbf{X}} - \mathbf{X}\right)\right\}$. It can be shown that this variable follows Gaussian distribution with zero mean. Its variance can be calculated as

$$\mathrm{E}\left\{v^2\right\} = \frac{N_0}{2}\|\hat{x} - x\|^2 = N_0\left(1 - \cos(\theta_\Delta)\right) \tag{28}$$

where $\theta_\Delta = \theta_m - \hat{\theta}_m$ is the phase difference between the transmitted symbol and incorrect decision. Also, the second equality follows from $\|\hat{x} - x\|^2 = \|\hat{x}\|^2 + \|x\|^2 - 2\mathrm{Re}\left\{\hat{x}^* x\right\} = 2\left(1 - \cos(\theta_\Delta)\right)$.

Therefore, the probability density function (PDF) of is given by

$$f(v) = \frac{1}{\sqrt{2\pi N_0\left(1 - \cos(\theta_\Delta)\right)}} e^{\left(\frac{-v^2}{2N_0\left(1-\cos(\theta_\Delta)\right)}\right)} \tag{29}$$

Replacing $\mathbf{X} = [x_1, x_2 ... x_N]^{\mathrm{T}}$ and $\hat{\mathbf{X}} = [\hat{x}_1, \hat{x}_2 ... \hat{x}_N]^{\mathrm{T}}$ in (24), we obtain

$$P\left(\mathbf{X} \to \hat{\mathbf{X}}\middle| \theta_{err}\right) = P\left(v > \mathrm{Re}\left\{e^{j\theta_{err}} - e^{j(\theta_{err}+\theta_\Delta)}\right\} \middle| \theta_{err}\right) \tag{30}$$

We write the conditional PEP as

$$P\left(\mathbf{X} \to \hat{\mathbf{X}}\middle| \theta_{err}\right) = P\left(v > \left[\cos(\theta_{err}) - \cos\left(\theta_{err} + \theta_\Delta\right)\right] \middle| \theta_{err}\right) \tag{31}$$

It can be re-written in terms of another function to simplify the rest of the analysis

$$P\left(\mathbf{X} \to \hat{\mathbf{X}}\middle| \theta_{err}\right) = Q\left(\frac{\left[\cos\left(\theta_{err}\right) - \cos\left(\theta_{err} + \theta_\Delta\right)\right]}{\sqrt{N_0\left(1 - \cos\left(\theta_\Delta\right)\right)}}\right) \tag{32}$$

where $Q(\cdot)$ is the Gaussian-Q function and general form in (33) is valid

$$P(X > x) = Q\left(\frac{x - \mu}{\sigma}\right) \tag{33}$$

As a sanity check, we will consider the case of no phase error. If we replace $\theta_{err} = 0$ in (31), the PEP reduces to the well-known expression for M-PSK [48]

$$P\left(\mathbf{X} \to \hat{\mathbf{X}}\middle| \theta_{err} = 0\right) = Q\left(\sqrt{\frac{1 - \cos\left(\theta_\Delta\right)}{N_0}}\right) = Q\left(\sqrt{\frac{d^2}{2N_0}}\right) \tag{34}$$

where d is the minimum distance between the symbols x and $\hat{x}$.

To find the unconditional PEP, we need to take expectation of (31) over θ_{err}. This yields

$$\mathrm{E}_{\theta_{err}}\left\{P\left(\mathbf{X}\rightarrow\hat{\mathbf{X}}\middle|\,\theta_{err}\right)\right\}=\int_{-\infty}^{\infty}Q\left(\frac{[\cos\left(\theta_{err}\right)-\cos\left(\theta_{err}+\theta_{\Delta}\right)]}{\sqrt{N_0\left(1-\cos\left(\theta_{\Delta}\right)\right)}}\right)f(\theta_{err})d\theta_{err} \quad (35)$$

which unfortunately does not yield a closed-form solution. In the following, we provide an approximate solution.

We first rewrite (31) as

$$P\left(\mathbf{X}\rightarrow\hat{\mathbf{X}}\middle|\,\theta_{err}\right)=Q\left(\frac{g(\theta_{err})}{a}\right) \quad (36)$$

where we define $g(\theta_{err})=\cos\left(\theta_{err}\right)-\cos\left(\theta_{err}+\theta_{\Delta}\right)$ and $a=\sqrt{N_0\left(1-\cos\left(\theta_{\Delta}\right)\right)}$. An improved version of Chernoff bound [49] is applied on (36) to approximate the Q function as

$$P\left(\mathbf{X}\rightarrow\hat{\mathbf{X}}\middle|\,\theta_{err}\right)\approx\frac{1}{12}e^{\frac{-g^2(\theta_{err})}{2a^2}}+\frac{1}{4}e^{\frac{-2g^2(\theta_{err})}{3a^2}} \quad (37)$$

We can now take the expectation of (37) over θ_{err} as

$$\mathrm{E}_{\theta_{err}}\left\{P\left(\mathbf{X}\rightarrow\hat{\mathbf{X}}\middle|\,\theta_{err}\right)\right\}\approx\frac{1}{12}\mathrm{E}_{\theta_{err}}\left\{e^{\frac{-g^2(\theta_{err})}{2a^2}}\right\}+\frac{1}{4}\mathrm{E}_{\theta_{err}}\left\{e^{\frac{-2g^2(\theta_{err})}{3a^2}}\right\} \quad (38)$$

These expectations are unfortunately still intractable. However, it is possible to show that the exponent terms can be approximately modeled by Gaussian distribution for the practical values under consideration. As a result, each exponential term can be approximated as a log-normal distribution. If $U=e^{\mu+\sigma Z}\sim LN\left(\mu,\sigma^2\right)$ where Z is a standard random variable, the expectation of U can be calculated as $\mathrm{E}\left\{\mathrm{U}\right\}=\mathrm{e}^{\mu+\sigma^2/2}$ [50]. By using this property, we can calculate the expectations in (38) as

$$\begin{aligned}\mathrm{E}_{\theta_{err}}\left\{P\left(\mathbf{X}\rightarrow\hat{\mathbf{X}}\middle|\,\theta_{err}\right)\right\}\approx&\frac{1}{12}\exp\left(\frac{-1}{2a^2}\mathrm{E}_{\theta_{err}}\left\{g^2(\theta_{err})\right\}+\frac{var\left\{g^2(\theta_{err})\right\}}{8a^4}\right)\\&+\frac{1}{4}\exp\left(\frac{-2}{3a^2}\mathrm{E}_{\theta_{err}}\left\{g^2(\theta_{err})\right\}+\frac{2var\left\{g^2(\theta_{err})\right\}}{9a^4}\right)\end{aligned} \quad (39)$$

The mean of the related θ_{err} terms are calculated as follows

$$\mathrm{E}_{\theta_{err}}\left\{g^2\left(\theta_{err}\right)\right\} = b_2\cos(2\theta_\Delta) - b_1\cos(\theta_\Delta) + b_0 \tag{40}$$

The variance of the related θ_{err} terms are calculated as follows

$$\begin{aligned} var_{\theta_{err}}\left\{g^2\left(\theta_{err}\right)\right\} &= \mathrm{E}_{\theta_{err}}\left\{g^4\left(\theta_{err}\right)\right\} - \mathrm{E}_{\theta_{err}}{}^2\left\{g^2\left(\theta_{err}\right)\right\} \\ &= c_4\cos(4\theta_\Delta) - c_3\cos(3\theta_\Delta) + c_2\cos(2\theta_\Delta) - c_1\cos(\theta_\Delta) + c_0 \end{aligned} \tag{41}$$

Replacing (40) and (41) in (39), the final form of the unconditional PEP can be written as

$$P\left(\mathbf{X} \rightarrow \hat{\mathbf{X}}\right) \approx \frac{1}{12}\exp\left\{\frac{1}{8a^4}\left(\left(\mathbf{c} - 4a^2\mathbf{b}\right)\mathbf{f}\right)\right\} + \frac{1}{4}\exp\left\{\frac{2}{9a^4}\left(\left(\mathbf{c} - 3a^2\mathbf{b}\right)\mathbf{f}\right)\right\} \tag{42}$$

where $\mathbf{f} = [f_0, f_1, f_2, f_3, f_4]^{\mathrm{T}}$, $\mathbf{c} = [c_0, c_1, c_2, c_3, c_4]$, and $\mathbf{b} = [b_0, b_1, b_2, 0, 0]$.

$$\mathbf{c} = \begin{bmatrix} 0.125e^{-8\sigma_{err}^2} - 0.875e^{-4\sigma_{err}^2} + 0.75 \\ 0.5e^{-8\sigma_{err}^2} - 1.5e^{-4\sigma_{err}^2} + 1 \\ 0.75e^{-8\sigma_{err}^2} - e^{-4\sigma_{err}^2} + 0.25 \\ 0.5e^{-8\sigma_{err}^2} - 0.5e^{-4\sigma_{err}^2} \\ 0.125e^{-8\sigma_{err}^2} - 0.125e^{-4\sigma_{err}^2} \end{bmatrix}^{\mathrm{T}} \tag{43}$$

$$\mathbf{b} = \begin{bmatrix} 0.5e^{-2\sigma_{err}^2} + 1 \\ e^{-2\sigma_{err}^2} + 1 \\ 0.5e^{-2\sigma_{err}^2} \\ 0 \\ 0 \end{bmatrix}^{\mathrm{T}} \tag{44}$$

$$\mathbf{f} = \begin{bmatrix} 1 \\ -\cos(\theta_\Delta) \\ \cos(2\theta_\Delta) \\ -\cos(3\theta_\Delta) \\ \cos(4\theta_\Delta) \end{bmatrix} \tag{45}$$

The union bound on symbol error rate (SER) can be expressed as [51]

$$P(e) < \frac{1}{M} \sum_{x} \sum_{\hat{x} \neq x} \frac{1}{12} \exp\left\{ \frac{1}{8a^4} \left(\left(\mathbf{c} - 4a^2 \mathbf{b} \right) \mathbf{f} \right) \right\} + \frac{1}{4} \exp\left\{ \frac{2}{9a^4} \left(\left(\mathbf{c} - 3a^2 \mathbf{b} \right) \mathbf{f} \right) \right\} \tag{46}$$

CHAPTER IV

NUMERICAL RESULTS

In this chapter, we investigate the accuracy of the derived PEP and present our numerical results for the error rate performance comparing analytical derivations with Monte Carlo simulations. We assume transmission of 4-PSK and 8-PSK signals. For 4-PSK, based on (3) and (4), the MZM modulating voltages are found as $v_{I,Q} \in \{-V_\pi/4, V_\pi/4\}$ (See Fig. 7). Similarly, the MZM parameters are found as $v_{I,Q} \in \{-V_\pi/2, -V_\pi/4, 0, V_\pi/4, V_\pi/2\}$ for 8-PSK.

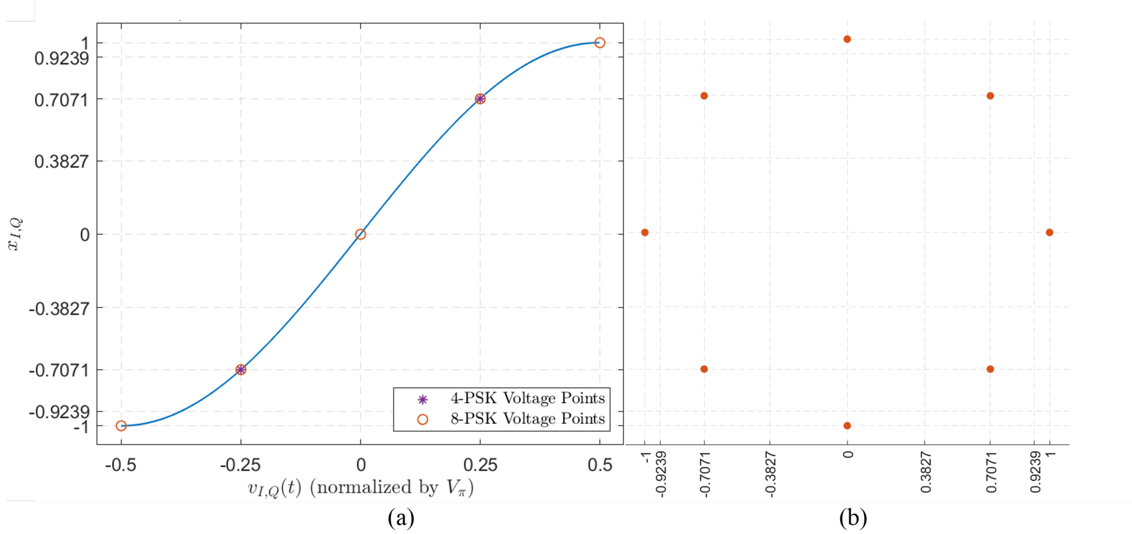

Figure 7: a) The relationship between MZM modulating voltages and symbol amplitudes b) Corresponding constellation diagram for PSK.

To illustrate the effect of phase noise and phase noise error on the constellation, received QPSK symbols are scattered on top of the transmitted symbols. As an example of $\Delta v = 100$ MHz and assuming a perfect channel, the constellation diagrams, before and after phase compansation methods are given in Fig. 8. Also, estimated and original phase noise values are tracked in terms of symbol timing.

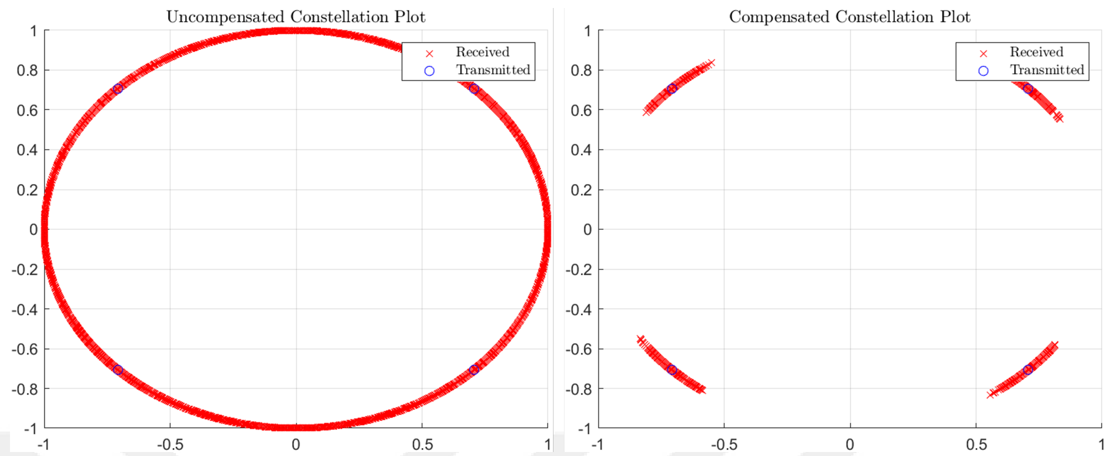

Figure 8: Constellation diagrams for uncompensated and compensated phase noise with $\Delta v = 100$ MHz, without channel noise.

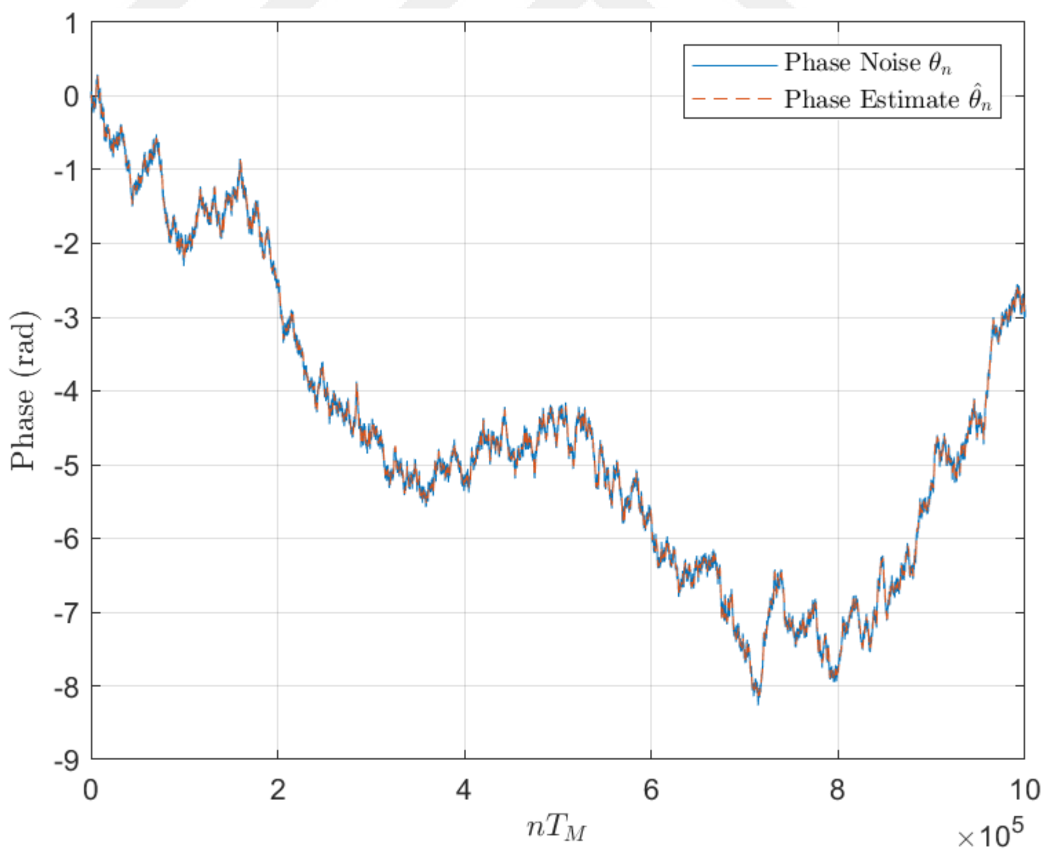

Figure 9: Phase noise and estimate in terms of symbol timing with $\Delta v = 100$ MHz, without channel noise.

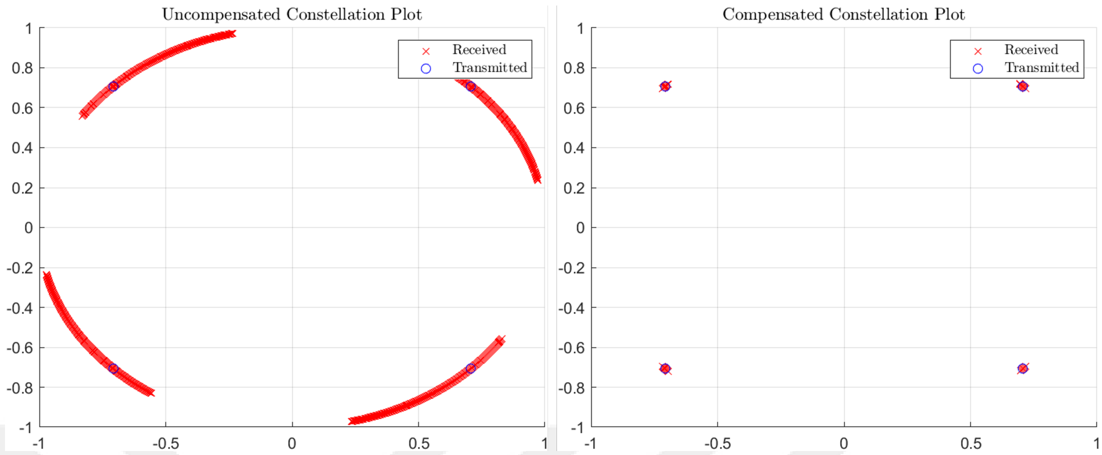

Figure 10: Constellation diagrams for uncompensated and compensated phase noise with $\Delta v = 1$ MHz, without channel noise.

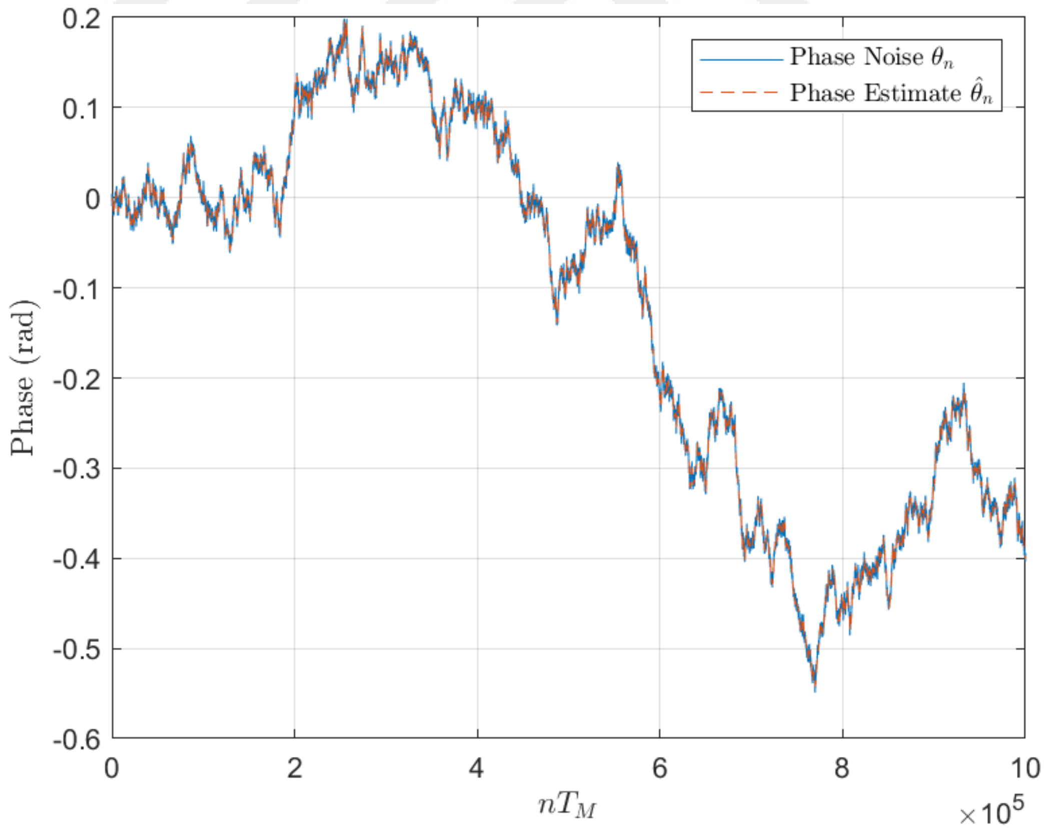

Figure 11: Phase noise and estimate in terms of symbol timing with $\Delta v = 1$ MHz, without channel noise.

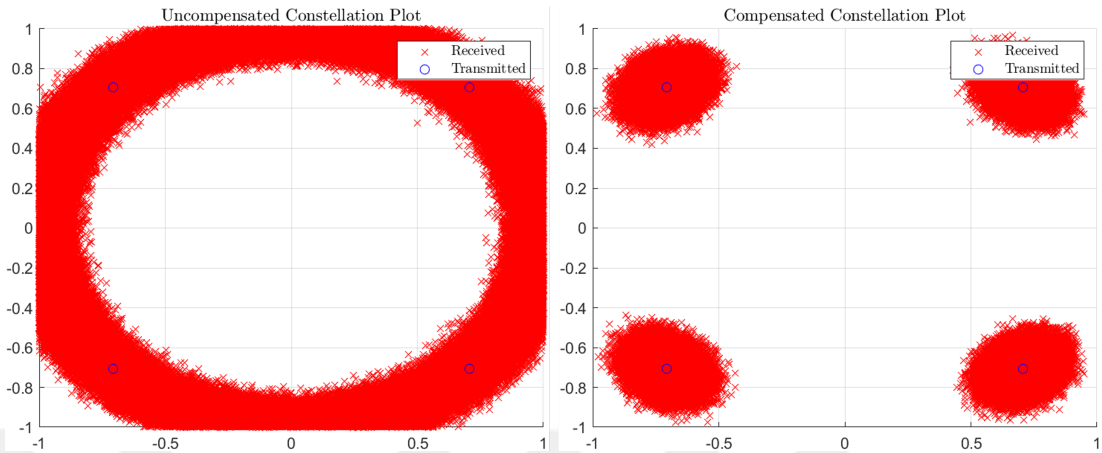

Figure 12: Constellation diagrams for uncompensated and compensated phase noise with $\Delta v = 100$ MHz and SNR=20 dB.

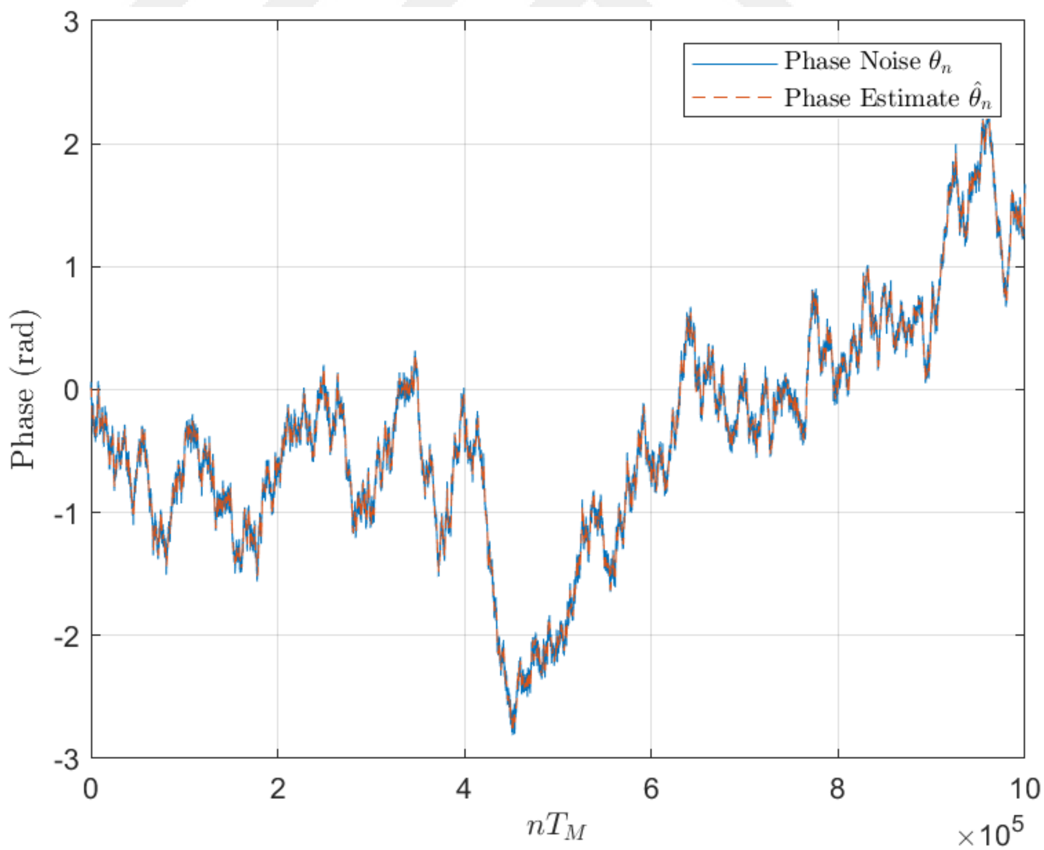

Figure 13: Phase noise and estimate in terms of symbol timing with $\Delta v = 100$ MHz and SNR=20 dB.

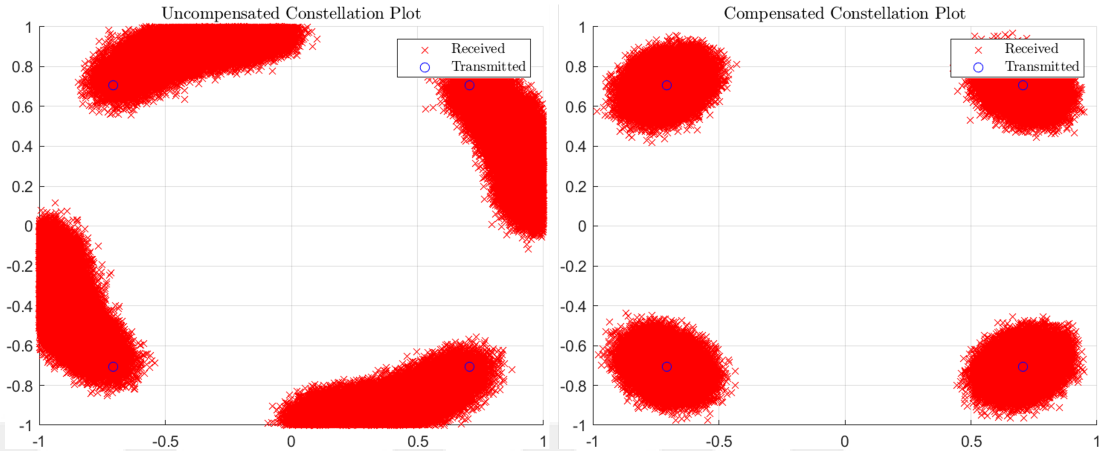

Figure 14: Constellation diagrams for uncompensated and compensated phase noise with $\Delta v = 1$ MHz and SNR=20 dB.

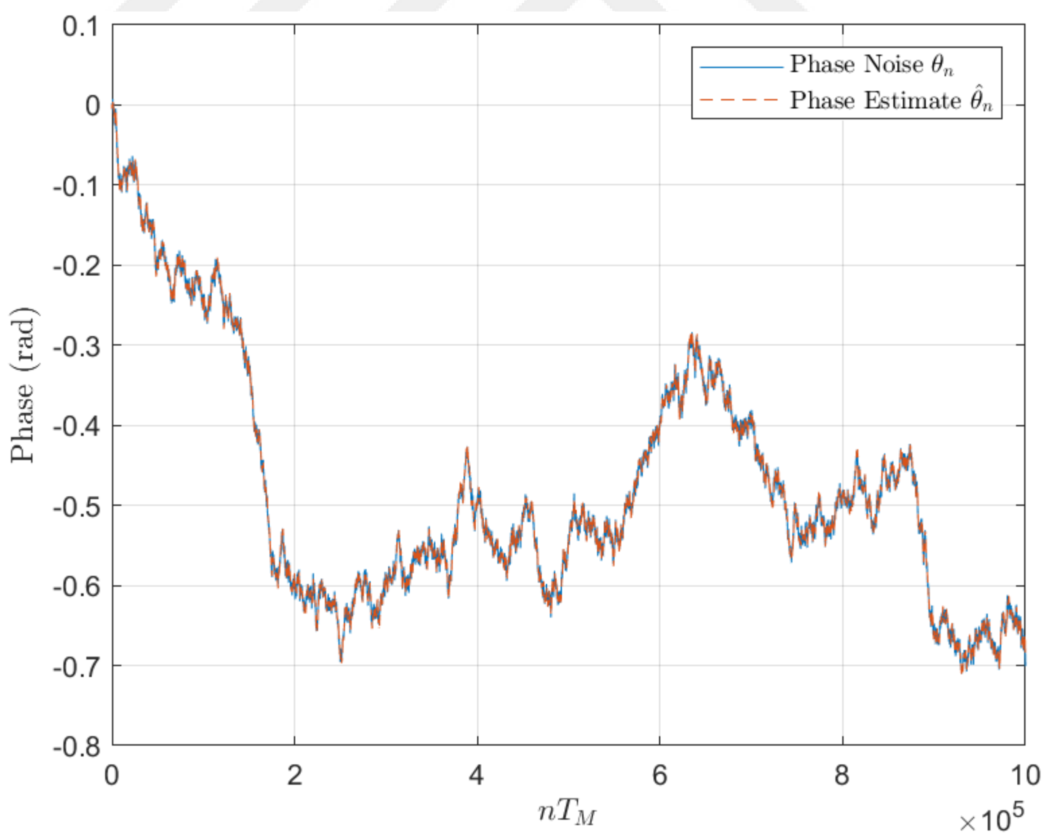

Figure 15: Phase noise and estimate in terms of symbol timing with $\Delta v = 1$ MHz and SNR=20 dB.

As seen in Fig. 9, the designed PLL is successfully locked and tracking the phase noise. Another example is given with $\Delta v = 1$ MHz. In Fig. 10, the constellations are present while Fig. 11 represents how well phase noise tracked. On top of the existing simulation parameters, an AWGN channel effect is included with SNR of 20 dB. The constellations and phase noise graphs are given in Fig. 12 and Fig. 13 for $\Delta v = 100$ MHz. Also repeated for $\Delta v = 1$ MHz as in Fig. 14 and Fig. 15.

These plots enable us to analyze the PLL performance related to the phase noise error. The first observation regarding to the linewidth of the laser can be done by comparing Fig. 8 and Fig. 10. While the pure phase noise with $\Delta v = 100$ MHz affects the symbol locations significantly and yields more error, $\Delta v = 1$ causes less rotations. On the other hand, Fig. 9 and Fig. 11 cannot be differentiated visibly. The same discussion can be done through comparing Fig. 12 and Fig. 14. In the noisy cases, there are some random distortions around the symbols. Nevertheless, the linewidth difference is not easily distinguishable on the compensated constellation plots due to AWGN noise.

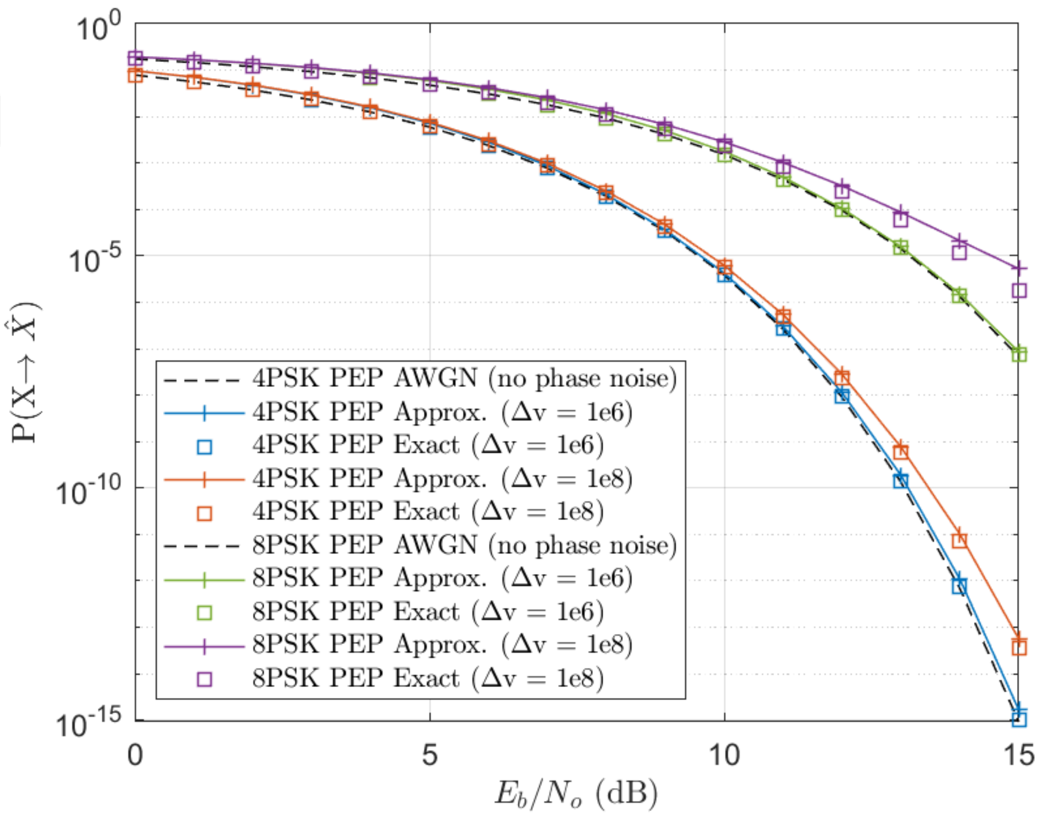

Figure 16: PEP for $M = 4$ and $M = 8$ at two different laser linewidths: $\Delta v = 1$ MHz and $\Delta v = 100$ MHz.

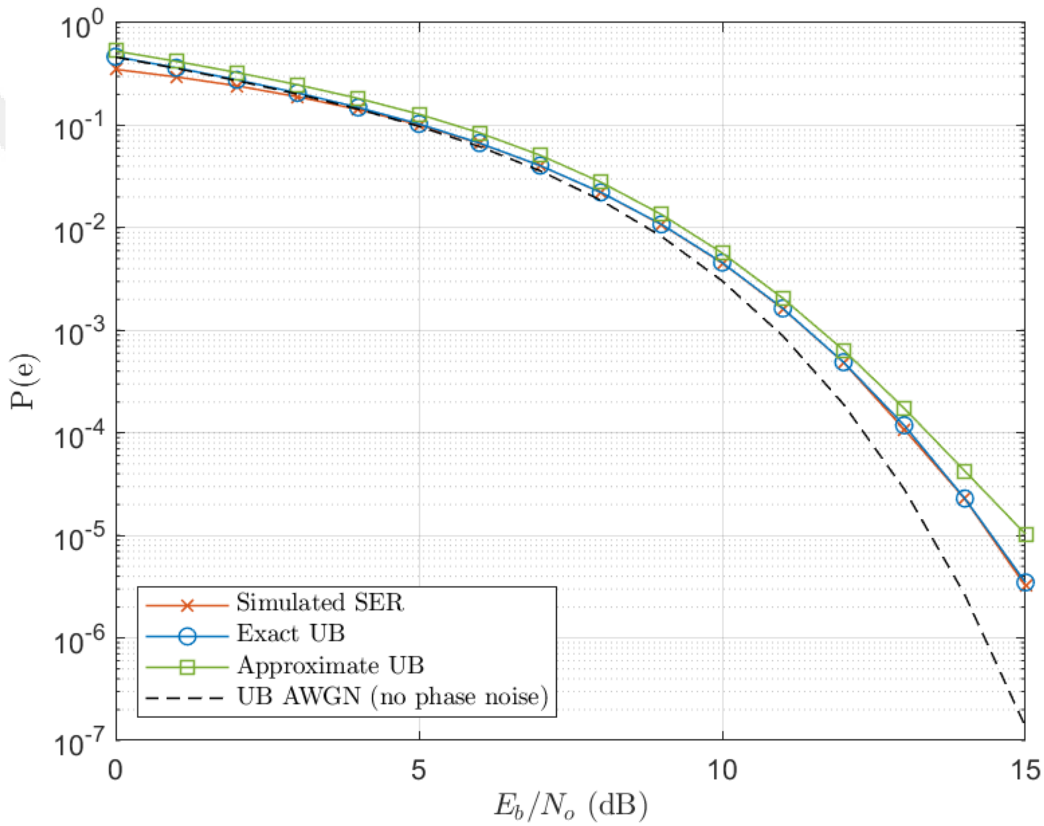

Figure 17: Symbol error rate performance for 8-PSK with laser linewidth of $\Delta v = 100$ MHz.

In Fig. 16, we plot PEP curves based on the derived approximate expression in (42). We consider laser linewidths of $\Delta v = 1$ MHz and $\Delta v = 100$ MHz. Based on the discussions in Section III, we choose $B_n = 6 \times 10^{-4}$ since it is an optimal value that can lock in both linewidths. To verify the accuracy of the derived expression, we also numerically evaluate the exact expression in (35) and present it as a benchmark. Our results demonstrate that there is a good match between the exact and approximate expressions for both modulation orders and the difference is less than 0.55 dB. To demonstrate the effect of phase noise, we further include (34) as another benchmark where only AWGN is assumed. It is observed that the degradation due to phase noise is negligibly small for a laser linewidth of $\Delta v = 1$ MHz. It becomes more pronounced for the laser linewidth of $\Delta v = 100$ MHz.

In Fig. 17, we present the union bound on the SER in (46) along with the Monte Carlo simulation results. For the calculation of the union bound, we consider both the exact PEP in (35) and derived PEP in (42). It is observed that the union bound based on the exact PEP converges to simulation results when the SNR is sufficiently high. On the other hand, the union bound based on the approximate PEP provides a tight upper bound. For instance, to achieve a targeted SER of 10^{-5}, SNR of 13.4 dB is required without any phase error. In the presence of residual phase noise, this increases to 15 dB indicating its degrading effect.

CHAPTER V

CONCLUSION

In conclusion, we have investigated the impact of laser phase noise on error performance for M-PSK modulation in coherent VLC. First, we demonstrated that the Gaussian assumption of phase error is valid for various PLL bandwidth values. Then, based on the statistical distribution of the residual phase, we derived a closed-form PEP expression using the log-normal approximation. The results are presented for numerically and approximately calculated PEP expressions. This was finally used to obtain a union bound on the SER which is shown to provide a tight bound on the performance. Overall, the analytical findings are compared with the benchmark within the SNR range of 0 to 15 dB. Through simulations, we validated the accuracy of the derived expression and quantified the impact of phase noise. Our results demonstrated that even the residual phase noise can bring degradations up to 1.6 dB for modulation sizes under consideration.

APPENDIX A

REAL-VALUED SIGNAL MODEL

In this appendix, we present the system modeling in non-complex domain. The goal is to prove that both the real and complex representations yield equivalent solutions. First of all, we recall the modulated M-PSK signal as follows

$$s_{out}(t) = \sqrt{2}\mathrm{Re}\left\{\tilde{s}_{out}(t)\right\} \tag{47}$$

where $\tilde{s}_{out} = x(t)e^{-j(2\pi f_c t+\theta_c(t))}$ is the complex envelope of the transmitted signal and $x(t) = x_I(t) - jx_Q(t) = e^{-j\theta_m(t)}$ is the baseband modulated signal. After this point, we utilize the real-valued representations of the signals. Accordingly, the real-valued modulated signal takes the following form

$$s_{out}(t) = \sqrt{2}x_I(t)\cos\left(2\pi f_c t + \theta_c(t)\right) - \sqrt{2}x_Q(t)\sin\left(2\pi f_c t + \theta_c(t)\right) \tag{48}$$

Next, the signal goes through the AWGN channel

$$r(t) = s_{out}(t) + n(t) \tag{49}$$

where $n(t)$ is a Gaussian random process. Followingly, when we substitute s_{out} in (48) into (49)

$$r(t) = \sqrt{2}\cos\left(\theta_m(t)\right)\cos\left(2\pi f_c t + \theta_c(t)\right) - \sqrt{2}\sin\left(\theta_m(t)\right)\sin\left(2\pi f_c t + \theta_c(t)\right) + n(t) \tag{50}$$

After that, we need to apply the optical mixer in real domain. To accomplish that the output of the local oscillator is exposed to $0°, 180°, 90°, 270°$ phase shifts, respectively.

$$\begin{bmatrix} c_{out,1}(t) \\ c_{out,2}(t) \\ c_{out,3}(t) \\ c_{out,4}(t) \end{bmatrix} = \frac{1}{2}\begin{bmatrix} r(t) + \sqrt{2}A_{LO}\cos\left(2\pi f_{LO}t + \theta_{LO}(t)\right) \\ r(t) - \sqrt{2}A_{LO}\cos\left(2\pi f_{LO}t + \theta_{LO}(t)\right) \\ r(t) + \sqrt{2}A_{LO}\sin\left(2\pi f_{LO}t + \theta_{LO}(t)\right) \\ r(t) - \sqrt{2}A_{LO}\sin\left(2\pi f_{LO}t + \theta_{LO}(t)\right) \end{bmatrix} \tag{51}$$

After the received signal is summed with the respective optical oscillator signals, the photodetector outputs are calculated based on the following operation

$$y_k(t) = R|c_{out,k}(t)|^2, k = 1, 2, 3, 4 \tag{52}$$

The outputs on each branch of the balanced coupler is calculated as

$$y_1(t) = \frac{R}{4}\left[r^2(t) + 2A_{LO}^2\cos^2(2\pi f_{LO}t + \theta_{LO}) + 2\sqrt{2}A_{LO}r(t)\cos(2\pi f_{LO}t + \theta_{LO})\right] \tag{53}$$

$$y_2(t) = \frac{R}{4}\left[r^2(t) + 2A_{LO}^2\cos^2(2\pi f_{LO}t + \theta_{LO}) - 2\sqrt{2}A_{LO}r(t)\cos(2\pi f_{LO}t + \theta_{LO})\right] \tag{54}$$

$$y_3(t) = \frac{R}{4}\left[r^2(t) + 2A_{LO}^2\sin^2(2\pi f_{LO}t + \theta_{LO}) + 2\sqrt{2}A_{LO}r(t)\sin(2\pi f_{LO}t + \theta_{LO})\right] \tag{55}$$

$$y_4(t) = \frac{R}{4}\left[r^2(t) + 2A_{LO}^2\sin^2(2\pi f_{LO}t + \theta_{LO}) - 2\sqrt{2}A_{LO}r(t)\sin(2\pi f_{LO}t + \theta_{LO})\right] \tag{56}$$

Finally, the outputs on I and Q branches are written by a simple substraction operation as in (57) and in (58)

$$\begin{aligned} y_I(t) &= y_1(t) - y_2(t) \\ &= R\sqrt{2}r(t)A_{LO}\cos\left(2\pi f_{LO}t + \theta_{LO}(t)\right) \end{aligned} \tag{57}$$

$$\begin{aligned} y_Q(t) &= y_3(t) - y_4(t) \\ &= R\sqrt{2}r(t)A_{LO}\sin\left(2\pi f_{LO}t + \theta_{LO}(t)\right) \end{aligned} \tag{58}$$

After substituing $r(t)$ in (47), the output signals are re-written, then re-arranged as in (56) and (57)

$$\begin{aligned}
y_I(t) &= R\sqrt{2}A_{LO}\cos\left(2\pi f_{LO}t+\theta_{LO}(t)\right)\begin{bmatrix}\sqrt{2}\cos\left(\theta_m(t)\right)\cos\left(2\pi f_c t+\theta_c(t)\right)\\ -\sqrt{2}\sin\left(\theta_m(t)\right)\sin\left(2\pi f_c t+\theta_c(t)\right)\\ +n(t)\end{bmatrix}\\
&= R\sqrt{2}A_{LO}\cos\left(2\pi f_{LO}t+\theta_{LO}(t)\right)\left[\sqrt{2}\cos\left(2\pi f_c t+\theta_c(t)+\theta_m(t)\right)+n(t)\right]\\
&= \sqrt{2}RA_{LO}\cos\left(2\pi f_{LO}t+\theta_{LO}(t)\right)n(t)\\
&\quad+2RA_{LO}\cos\left(2\pi f_{LO}t+\theta_{LO}(t)\right)\cos\left(2\pi f_c t+\theta_c(t)+\theta_m(t)\right)\\
&= \sqrt{2}RA_{LO}\cos\left(2\pi f_{LO}t+\theta_{LO}(t)\right)n(t)\\
&\quad+RA_{LO}\cos\left(2\pi f_{LO}t+2\pi f_c t+\theta_c(t)+\theta_m(t)+\theta_{LO}(t)\right)\\
&\quad+RA_{LO}\cos\left(2\pi f_{LO}t-2\pi f_c t+\theta_{LO}(t)-\theta_c(t)-\theta_m(t)\right)
\end{aligned}\tag{59}$$

$$\begin{aligned}
y_Q(t) &= R\sqrt{2}A_{LO}\sin\left(2\pi f_{LO}t+\theta_{LO}(t)\right)\begin{bmatrix}\sqrt{2}\cos\left(\theta_m(t)\right)\cos\left(2\pi f_c t+\theta_c(t)\right)\\ -\sqrt{2}\sin\left(\theta_m(t)\right)\sin\left(2\pi f_c t+\theta_c(t)\right)\\ +n(t)\end{bmatrix}\\
&= R\sqrt{2}A_{LO}\sin\left(2\pi f_{LO}t+\theta_{LO}(t)\right)\left[\sqrt{2}\cos\left(2\pi f_c t+\theta_c(t)+\theta_m(t)\right)+n(t)\right]\\
&= \sqrt{2}RA_{LO}\sin\left(2\pi f_{LO}t+\theta_{LO}(t)\right)n(t)\\
&\quad+2RA_{LO}\sin\left(2\pi f_{LO}t+\theta_{LO}(t)\right)\cos\left(2\pi f_c t+\theta_c(t)+\theta_m(t)\right)\\
&= \sqrt{2}RA_{LO}\sin\left(2\pi f_{LO}t+\theta_{LO}(t)\right)n(t)\\
&\quad+RA_{LO}\sin\left(2\pi f_{LO}t+2\pi f_c t+\theta_c(t)+\theta_m(t)+\theta_{LO}(t)\right)\\
&\quad+RA_{LO}\sin\left(2\pi f_{LO}t-2\pi f_c t+\theta_{LO}(t)-\theta_c(t)-\theta_m(t)\right)
\end{aligned}\tag{60}$$

If the frequencies of the local oscillators at transmitter and receiver are equal, $f_{LO} = f_c$, the output current signals vary accordingly. Thus, (56) and (57) are modified as follows

$$\begin{aligned} y_I(t) = \sqrt{2}RA_{LO}\cos\left(2\pi f_{LO}t + \theta_{LO}(t)\right)n(t) \\ + RA_{LO}\cos\left(4\pi f_{LO}t + \theta_c(t) + \theta_m(t) + \theta_{LO}(t)\right) \\ + RA_{LO}\cos\left(\theta_{LO}(t) - \theta_c(t) - \theta_m(t)\right) \end{aligned} \tag{61}$$

$$\begin{aligned} y_Q(t) = \sqrt{2}RA_{LO}\sin\left(2\pi f_{LO}t + \theta_{LO}(t)\right)n(t) \\ + RA_{LO}\sin\left(4\pi f_{LO}t + \theta_c(t) + \theta_m(t) + \theta_{LO}(t)\right) \\ + RA_{LO}\sin\left(\theta_{LO}(t) - \theta_c(t) - \theta_m(t)\right) \end{aligned} \tag{62}$$

As seen, a double frequency term, $4f_{LO}$, and intermediate frequency (IF) term appear similar to RF case. However, they were not present in the complex domain implementation at any step (see Equation (13), (14) and after).

In contrast to this conventional mathematical transmission, operations are different in the coherent detection. An optical front-end acts as an optical mixer and combines the electrical fields of the local laser and the incoming signals. The envelope of the resulting signal can beat with each other to form sum and difference of the frequencies. Then, this combined signal is received by a photodetector (PD). However, PD has a limited operational frequency band which allows only the lower frequency term to pass through. Therefore, PD filters out the high frequencies (double frequency terms) and this is already implemented in the complex notation since we are left with the IF only [52].

REFERENCES

[1] T. Cogalan and H. Haas, “Why would 5g need optical wireless communications?,” in *2017 IEEE 28th Annual International Symposium on Personal, Indoor, and Mobile Radio Communications (PIMRC)*, pp. 1–6, IEEE, 2017.

[2] M. Kavehrad, “Optical wireless applications: a solution to ease the wireless airwaves spectrum crunch,” in *Broadband Access Communication Technologies VII*, vol. 8645, p. 86, International Society for Optics and Photonics, SPIE, 2013.

[3] Y. Wang, G. Zhao, K. Xu, Y. Shen, C. Xu, M. Hassan, and W. Hu, “Ev-dmd: a high-speed vlc system,” in *Proceedings of the ACM SIGCOMM 2023 Conference*, pp. 1168–1169, 2023.

[4] R. Ji, S. Wang, Q. Liu, and W. Lu, “High-speed visible light communications: Enabling technologies and state of the art,” *Applied Sciences*, vol. 8, no. 4, p. 589, 2018.

[5] H. Parikh, J. Chokshi, N. Gala, and T. Biradar, “Wirelessly transmitting a grayscale image using visible light,” in *2013 international conference on advances in technology and engineering (ICATE)*, pp. 1–6, IEEE, 2013.

[6] S. Zhao, J. Xu, and O. Trescases, “A dimmable led driver for visible light communication (vlc) based on llc resonant dc-dc converter operating in burst mode,” in *2013 Twenty-Eighth Annual IEEE Applied Power Electronics Conference and Exposition (APEC)*, pp. 2144–2150, IEEE, 2013.

[7] H. Ma, L. Lampe, and S. Hranilovic, “Integration of indoor visible light and power line communication systems,” in *2013 IEEE 17th International Symposium on Power Line Communications and Its Applications*, pp. 291–296, IEEE, 2013.

[8] N. Chi, Y. Zhou, Y. Wei, and F. Hu, “Visible light communication in 6g: Advances, challenges, and prospects,” *IEEE Vehicular Technology Magazine*, vol. 15, no. 4, pp. 93–102, 2020.

[9] R. Kisacik, M. Y. Yagan, M. Uysal, A. E. Pusane, and A. D. Yalcinkaya, “A new led response model and its application to pre-equalization in vlc systems,” *IEEE Photonics Technology Letters*, vol. 33, no. 17, pp. 955–958, 2021.

[10] W. Niu, Z. Xu, Y. Liu, X. Lin, J. Cai, J. Shi, X. Wang, G. Wang, J. Zhang, F. Jiang, Z. He, S. Yu, C. Shen, J. Zhang, and N. Chi, “Key technologies for high-speed si-substrate led based visible light communication,” *Journal of Lightwave Technology*, vol. 41, no. 11, pp. 3316–3331, 2023.

[11] E. Semaan, E. Tejedor, R. K. Kochhar, S. Magnusson, and S. Parkvall, "6g spectrum - enabling the future mobile life beyond 2030," tech. rep., Ericsson Inc., March 2023.

[12] L. Ulrich, "Bmw laser headlights slice through the dark," tech. rep., IEEE Spectrum, October 2013.

[13] F. Rahman, "Lighting with lasers," *"Optics & Photonics News"*, vol. 31, pp. 44–51, Jul 2020.

[14] F. Zafar, M. Bakaul, and R. Parthiban, "Laser-diode-based visible light communication: Toward gigabit class communication," *IEEE Communications Magazine*, vol. 55, no. 2, pp. 144–151, 2017.

[15] T.-C. Wu, Y.-C. Chi, H.-Y. Wang, C.-T. Tsai, Y.-F. Huang, and G.-R. Lin, "Tricolor r/g/b laser diode based eye-safe white lighting communication beyond 8 gbit/s," *Scientific reports*, vol. 7, no. 1, p. 11, 2017.

[16] C. Lee, C. Shen, H. M. Oubei, M. Cantore, B. Janjua, T. K. Ng, R. M. Farrell, M. M. El-Desouki, J. S. Speck, S. Nakamura, *et al.*, "2 gbit/s data transmission from an unfiltered laser-based phosphor-converted white lighting communication system," *Optics express*, vol. 23, no. 23, pp. 29779–29787, 2015.

[17] Y.-C. Chi, D.-H. Hsieh, C.-Y. Lin, H.-Y. Chen, C.-Y. Huang, J.-H. He, B. Ooi, S. P. DenBaars, S. Nakamura, H.-C. Kuo, *et al.*, "Phosphorous diffuser diverged blue laser diode for indoor lighting and communication," *Scientific reports*, vol. 5, no. 1, pp. 1–9, 2015.

[18] H. Chun, S. Rajbhandari, D. Tsonev, G. Faulkner, H. Haas, and D. O'Brien, "Visible light communication using laser diode based remote phosphor technique," in *2015 IEEE International Conference on Communication Workshop (ICCW)*, pp. 1392–1397, 2015.

[19] C. Lee, M. S. Islim, S. Videv, A. Sparks, B. Shah, P. Rudy, M. McLaurin, H. Haas, and J. Raring, "Advanced lifi technology: laser light," in *Light-emitting devices, materials, and applications XXIV*, vol. 11302, pp. 116–123, SPIE, 2020.

[20] C. Lee, M. S. Islim, S. Das, A. Spark, S. Videv, P. Rudy, B. Shah, M. McLaurin, H. Haas, and J. Raring, "26 gbit/s lifi system with laser-based white light transmitter," *Journal of Lightwave Technology*, vol. 40, no. 5, pp. 1432–1439, 2021.

[21] S. Kumar and M. J. Deen, *Fiber optic communications: fundamentals and applications.* John Wiley Sons, 2014.

[22] M. Uysal and H. Nouri, "Optical wireless communications—an emerging technology," in *2014 16th international conference on transparent optical networks (ICTON)*, pp. 1–7, IEEE, 2014.

[23] J. Li and M. Uysal, "Optical wireless communications: system model, capacity and coding," in *2003 IEEE 58th Vehicular Technology Conference. VTC 2003-Fall (IEEE Cat. No.03CH37484)*, vol. 1, pp. 168–172 Vol.1, 2003.

[24] M. A. Arfaoui, M. D. Soltani, I. Tavakkolnia, A. Ghrayeb, M. Safari, C. M. Assi, and H. Haas, "Physical layer security for visible light communication systems: A survey," *IEEE Communications Surveys & Tutorials*, vol. 22, no. 3, pp. 1887–1908, 2020.

[25] D. Karunatilaka, F. Zafar, V. Kalavally, and R. Parthiban, "Led based indoor visible light communications: State of the art," *IEEE communications surveys & tutorials*, vol. 17, no. 3, pp. 1649–1678, 2015.

[26] M. Saadi and L. Wuttisittikulkij, "Visible light communication–the journey so far," *Journal of Optical Communications*, vol. 40, no. 4, pp. 447–453, 2019.

[27] S. I. Mushfique, P. Palathingal, Y. S. Eroglu, M. Yuksel, I. Guvenc, and N. Pala, "A software-defined multi-element vlc architecture," *IEEE Communications Magazine*, vol. 56, no. 2, pp. 196–203, 2018.

[28] L. E. M. Matheus, A. B. Vieira, L. F. Vieira, M. A. Vieira, and O. Gnawali, "Visible light communication: concepts, applications and challenges," *IEEE Communications Surveys & Tutorials*, vol. 21, no. 4, pp. 3204–3237, 2019.

[29] N. Suzuki, H. Miura, K. Mochizuki, and K. Matsuda, "Simplified digital coherent-based beyond-100g optical access systems for b5g/6g," *Journal of Optical Communications and Networking*, vol. 14, no. 1, pp. A1–A10, 2022.

[30] H.-B. Jeon, S.-M. Kim, H.-J. Moon, D.-H. Kwon, J.-W. Lee, J.-M. Chung, S.-K. Han, C.-B. Chae, and M.-S. Alouini, "Free-space optical communications for 6g wireless networks: Challenges, opportunities, and prototype validation," *IEEE Communications Magazine*, vol. 61, no. 4, pp. 116–121, 2023.

[31] S. Watson, M. Tan, S. P. Najda, P. Perlin, M. Leszczynski, G. Targowski, S. Grzanka, and A. Kelly, "Visible light communications using a directly modulated 422 nm gan laser diode," *Optics letters*, vol. 38, no. 19, pp. 3792–3794, 2013.

[32] B. Janjua, H. M. Oubei, J. R. D. Retamal, T. K. Ng, C.-T. Tsai, H.-Y. Wang, Y.-C. Chi, H.-C. Kuo, G.-R. Lin, J.-H. He, *et al.*, "Going beyond 4 gbps data rate by employing rgb laser diodes for visible light communication," *Optics express*, vol. 23, no. 14, pp. 18746–18753, 2015.

[33] C. Lee, C. Zhang, M. Cantore, R. M. Farrell, S. H. Oh, T. Margalith, J. S. Speck, S. Nakamura, J. E. Bowers, and S. P. DenBaars, "4 gbps direct modulation of 450 nm gan laser for high-speed visible light communication," *Optics express*, vol. 23, no. 12, pp. 16232–16237, 2015.

[34] Y.-C. Chi, D.-H. Hsieh, C.-T. Tsai, H.-Y. Chen, H.-C. Kuo, and G.-R. Lin, "450-nm gan laser diode enables high-speed visible light communication with 9-gbps qam-ofdm," *Optics express*, vol. 23, no. 10, pp. 13051–13059, 2015.

[35] C.-T. Tsai, C.-H. Cheng, H.-C. Kuo, and G.-R. Lin, "Toward high-speed visible laser lighting based optical wireless communications," *Progress in Quantum Electronics*, vol. 67, p. 100225, 2019.

[36] K. A. Denault, M. Cantore, S. Nakamura, S. P. DenBaars, and R. Seshadri, "Efficient and stable laser-driven white lighting," *Aip Advances*, vol. 3, 07 2013.

[37] C. Henry, "Phase noise in semiconductor lasers," *Journal of Lightwave Technology*, vol. 4, no. 3, pp. 298–311, 1986.

[38] S. Ishimura, Y. Nakano, and T. Tanemura, "Impact of laser phase noise on self-coherent transceivers employing high-order qam formats," *Journal of Lightwave Technology*, vol. 39, no. 19, pp. 6150–6158, 2021.

[39] J. P. Santacruz, S. Rommel, U. Johannsen, A. Jurado-Navas, and I. T. Monroy, "Analysis and compensation of phase noise in mm-wave ofdm arof systems for beyond 5g," *Journal of Lightwave Technology*, vol. 39, no. 6, pp. 1602–1610, 2021.

[40] X. Zhou, Y. Gao, J. Huo, and W. Shieh, "Theoretical analysis of phase noise induced by laser linewidth and mismatch length in self-homodyne coherent systems," *J. Lightwave Technol.*, vol. 39, pp. 1312–1321, Mar 2021.

[41] L. Paillier, R. Le Bidan, J.-M. Conan, G. Artaud, N. Védrenne, and Y. Jaouën, "Space-ground coherent optical links: Ground receiver performance with adaptive optics and digital phase-locked loop," *Journal of Lightwave Technology*, vol. 38, no. 20, pp. 5716–5727, 2020.

[42] M. Naghshvarianjahromi, S. Kumar, and M. J. Deen, "Free space ground to satellite optical communications using kramers–kronig transceiver in the presence of atmospheric turbulence," *Sensors*, vol. 22, no. 9, p. 3435, 2022.

[43] A. M. Wyglinski, R. Getz, T. Collins, and D. Pu, *Software-defined radio for engineers*. Artech House, 2018.

[44] Q. M. Chaudhari, *Wireless Communications from the Ground Up: An SDR Perspective*. CreateSpace Independent Publishing Platform, 2018.

[45] D. A. de Arruda Mello and F. A. Barbosa, *Digital Coherent Optical Systems. ON*. Springer, 2021.

[46] H. Arslan, *Wireless Communication Signals: A Laboratory-Based Approach*. Wiley, 2021.

[47] M. Rice, *Digital communications: a discrete-time approach*. Pearson, 2009.

[48] S. Benedetto and E. Biglieri, *Principles of digital transmission: with wireless applications*. Springer Science & Business Media, 1999.

[49] M. Chiani, D. Dardari, and M. K. Simon, "New exponential bounds and approximations for the computation of error probability in fading channels," *IEEE Transactions on Wireless Communications*, vol. 2, no. 4, pp. 840–845, 2003.

[50] R. B. Leipnik, "On lognormal random variables: I-the characteristic function," *The Journal of the Australian Mathematical Society. Series B. Applied Mathematics*, vol. 32, no. 3, p. 327–347, 1991.

[51] M. K. Simon and M.-S. Alouini, *Digital communication over fading channels*. Wiley Series in Telecommunications and Signal Processing, 2005.

[52] L. N. Binh, *Optical Fiber Communication Systems with MATLAB and Simulink Models*. CRC Press, 2015.

VITA

Zeynep Özbilgin obtained her Bachelor's degree in Electrical and Electronics Engineering with high honors from Istanbul Medipol University in June 2022. Following August, she entered Ozyegin University for Master of Science degree in Electrical and Electronics Engineering. She is currently working in communication systems engineering with the Communication Theory and Technologies (CT&T) Research Group at the Ozyegin University, Istanbul, Turkey. Her main research interests include wireless communication, coherent visible light communication, and deep learning.